University of Nottingham
UK | CHINA | MALAYSIA

Master Thesis

2022/23

Optimized Drop-on-demand Printing Path Strategies for Curved Shapes

UNIVERSITY OF NOTTINGHAM NINGBO CHINA

Name: Dongsheng SHI

Student ID: 20513684

Lead Supervisor: Dr. Adam Rushworth

Second Supervisor: Dr. Hao Chen

Third Supervisor: Dr. Guang Li

Fourth Supervisor: Dr. Yi Nie

Abstract

Additive manufacturing is considered one of the revolutionary production technologies, and an appropriate deposition path for metal droplets is critical in additive manufacturing, which contributes to the printing at high quality. Therefore, optimizing the planning process is of vital importance, and this research proposed an appropriate method for printing curved shapes to reduce layer surface height variation and roughness. Depending on various curvatures with internal filling, an adaptive spacing with angular displacement was determined, in the balancing of improving dimensional accuracy and reducing material consumption. In addition, dynamic changes in the droplet energy and the droplet deposition radius at different release heights were obtained, as a basis for the spacing of neighboring droplets in the path planning. The components of the printing system for high-melting-point metals were integrated, and therefore the system operation could be supported in the compatible software and hardware. Based on the drop-on-demand technique, two-dimensional curved patterns were printed, and three-dimensional curved objects with the internal filling were completely manufactured. Compared to common path planning methods, the result showed the surface flatness was improved by more than 30% based on the proposed strategies. The proposed method approximated the curved contours, and the filled rate was close to 90% in spite of the cross-sectional radius of the printed objects was small, less than 5 mm. The strategies proposed in this research were proven to be effective, laying the foundation for the practical application of droplet-based manufacturing technology.

Table of Content

Table of Figures

Table of Tables

Abbreviations

2D	Two Dimensional
3D	Three Dimensional
AM	Additive Manufacturing
CAD	Computer Aided Design
DOD	Drop-on-Demand
FDM	Fused Deposition Modeling
BJ	Binder Jetting
SLM	Selective Laser Melting
SLS	Selective Laser Sintering
STL	Standard Tessellation Language
G-code	Geometric Code
CNC	Computer Numerical Control
FFF	Fused-filament-fabrication
ABB	Asea Brown Boveri
FPGA	Field Programmable Gate Array
PBF	Powder Bed Fusion
DED	Direct Energy Deposition
PID	Product, integration, derivation
I/O	Input/Output
VOF	Volume of Fluid

Chapter 1 Introduction

1.1 Background

1.1.1 Additive layer manufacturing

Additive-layer Manufacturing (AM) is considered one of the revolutionary production technologies due to its versatility. In manufacturing, 3D printing can increase efficiency and sustainability at the supply chain end [1]. Additively manufactured parts supplied to the automobile and aerospace sectors constitute roughly 20 percent of the overall additive manufacturing market [2]. In a report, the AM market is expected to yield components and final products, worth $2 trillion by 2030 [3]. Therefore, the use of reliable production technologies combined with low-cost manufacturing processes to produce products will be a feasible strategy for the industry of the future.

There are various printing techniques such as Binder Jetting (BJ), Selective Laser Melting (SLM), Selective Laser Sintering (SLS), and Fused Deposition Modeling (FDM) that can handle a range of materials [4]. For BJ, binders enter a bed of raw powder [5]. Mechanical properties of the printed parts based on BJ are limited due to fragility, and post-processing in the form of casting or sintering is required. In SLM or SLS, metal powders are selectively melted or sintered using high power lasers. The parts manufactured by SLM or SLS are prone to porous surfaces and poor surface finishes [6, 7]. In addition, over half of products are fabricated using polymer-plastic filaments based on additive manufacturing [8]. Overall, additive manufacturing reduces the steps of traditional manufacturing and builds parts without geometric constraints, which shows the great potential [9].

1.1.2 Metal-droplet on demand 3D printing

As one of novel manufacturing techniques, metal droplet-based additive manufacturing, has attracted attention on account of advantages such as low cost and high efficiency in energy consumption. Gao and Sonin [10] first utilized molten droplets as the units for additive manufacturing. Luo et al. [11] proposed a new type of on-demand metal droplet generation device. The repeated electromagnetic force generated by the input pulse voltage drives an impact rod. Then the impact rod strikes the heat-resistant vibration transfer rod, pushing individual droplets out of the nozzle. Based on the optical images of 3D-printed particles, the effect of the pulse duration on the size of ejected droplets was analyzed. The results indicate that shorter pulse widths could reduce the droplet size. Luo et al. selected the metal material of Sn-40 wt% Pb, which requires pretreatment (remove metal oxide skin by grinding) before being utilized. Since Sn-40 wt% Pb is widely applied in the electronics area, it was also adopted by Dou et al. [12]. The melting point of the manufacturing material Sn-40 wt% is 456 K (183 ℃), and the solidification behavior on the substrate platform was tested in an argon gas environment. Dou et al. used a piezoelectric actuator and a crucible for drop-on-demand manufacturing. The observation techniques such as scanning electron microscopes, optical measuring microscopes, and industrial digital cameras were used to observe the solidified and combined form of the metal droplets. The solidification time was more sensitive to different temperatures of the substrate, which was from 0.46 to 4.72 s, while the droplet adhesion varied little with temperature. At the same substrate temperature, the expansion of droplet spacing increased the risk of metal line fracture, as shown in Figure 1.

Figure 1. Metal line fracture [12].

For metal droplets heated at high temperatures (>500 ℃), Simonelli et al. [13] inductively heated Sn or Ag metals, and liquid droplets were created by a push force. Plates of 99.9% Cu were selected as the deposition substrate, and the influence of substrate selection on adhesion has been studied. According to the research by Meda et al. [14], aluminum alloy 4043 wire was heated at 900 °C in a

resistively heated crucible. The metal droplets were deposited on a polyimide substrate, as shown in Figure 2. Droplet production frequency and spacing were changed to analyze the influence on the electrical resistivity of the deposition lines.

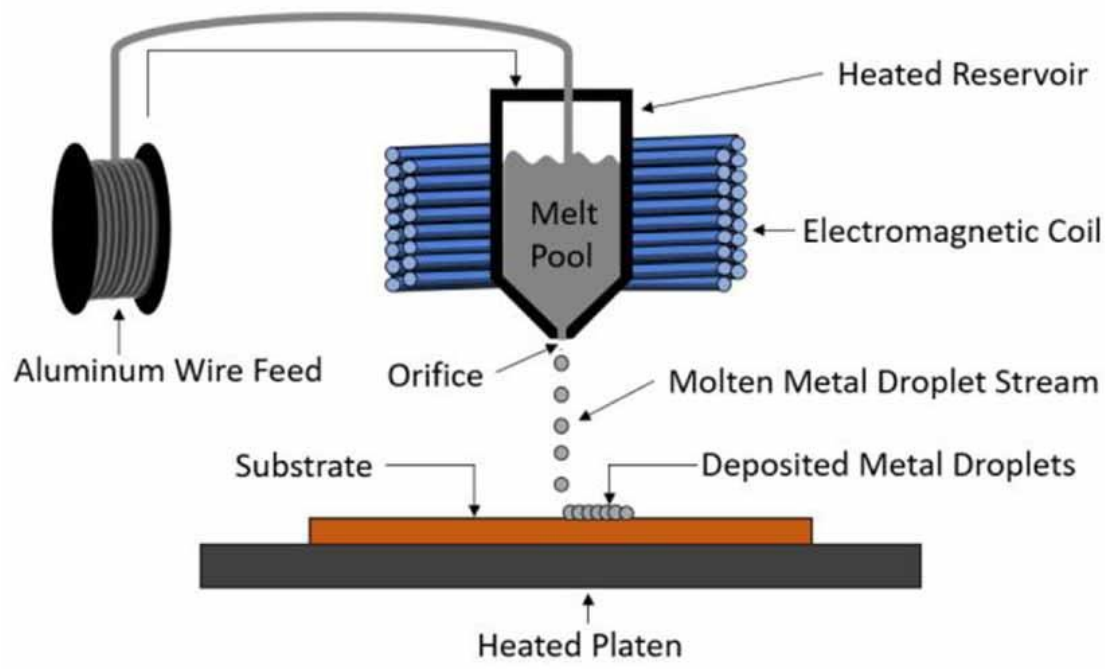

Figure 2. Metal-droplet system [14].

1.1.3 Process of the metal-droplet on demand 3D printing

The metal-droplet on demand manufacturing involves product design, processing and fabricating. In the early stage of additive manufacturing, a diagram of the 3D model is required, which contains the spatial Cartesian coordinates, periphery and internal contours of the 3D model to be printed. This model data is then utilized and processed, which can be also used as input for slicing.

For the reference and subsequent slicing, 3D models to be printed are usually drawn in a modelling software in three dimensions. Since computer-aided design (CAD) software is based on classic and basic two-dimensional drawing, it

is used for two-dimensional patterns. SolidWorks is user friendly, and it is generally used for small to medium sized printed models. Other mainstream software used for additive manufacturing contains UG, CATIA and Creo. Creo is widely applied in industries requiring three-dimensional components, while UG is generally used by medium or large enterprises to build complex models. At present, all 3D modelling software is well established and functional. The user-friendly operation makes model design easier and faster.

After the model design and drawing, the exported file format is also related to the success of manufacturing [15]. A mismatched file format can not be identified by the slicing software, such as Ultimaker Cura. An unsuitable file format can also result in incomplete raw data in slices, overlapping shapes and surface breakage. Therefore, the exported file format can be Standard Tessellation Language (STL), which can be identified by slicing software. The STL format was developed as a graphic type for the technical services of layered manufacturing. The STL format utilizes triangular meshes to describe a model in three dimensions, expressing the geometric information of the three-dimensional object without providing or supporting auxiliary information such as colour and material [16], [17]. There are two forms of STL files, text (ASCII format) and binary (BINARY), and the ASCII format is more generic than the BINARY format. The STL output data is simplified, and the format is manageable, and hence the STL format is widely used as a simplified version of a 3D model.

Šljivić et al. compared printed objects based on a technique of Fused Deposition Modeling, using three slicing software, Simplify3D, Slic3r, and Ultimaker Cura [18]. For lower-cost 3D printers, free open-source software is available, containing Slic3r and Ultimaker Cura. Šljivić et al. indicated that Ultimaker Cura sliced better than Slic3r, and the error between the expected model and the printed part sliced by Slic3r was greater than 6.7%.

For specific 3D printing systems and consumables, the manufacturing parameters can be configured and modified in the optimized slicing software. Industry-standard integrated software streamlines workflows for greater

productivity, and slicing software integrates with material manufacturing printers and consumables. In practical terms, the custom configuration in the slicing software can be modified to match the designated printing system. The slicing software such as Ultimaker Cura is available as open-source software, completely free of charge across platforms, and supports the system running on Linux, Windows, and Mac. A range of custom parameters allow for manual control, and reliable connection of hardware and materials. More features can be added to the slicing software, with the support for reading OBJ, X3D, and 3MF file formats.

Printed models can be interpreted by slicing software into Geometric Code (G-code) containing slicing layers and paths, as shown in Figure 3. The slicing software reads the various parts of the imported model and divide it into smaller parts. The settings can be adjusted as required and a file is saved that is compatible with the Computer Numerical Control (CNC) system, which was used in the project. A networked 3D printer can read the file remotely and control the printing, or the file can be saved to a USB stick or SD card and transferred to a local printer.

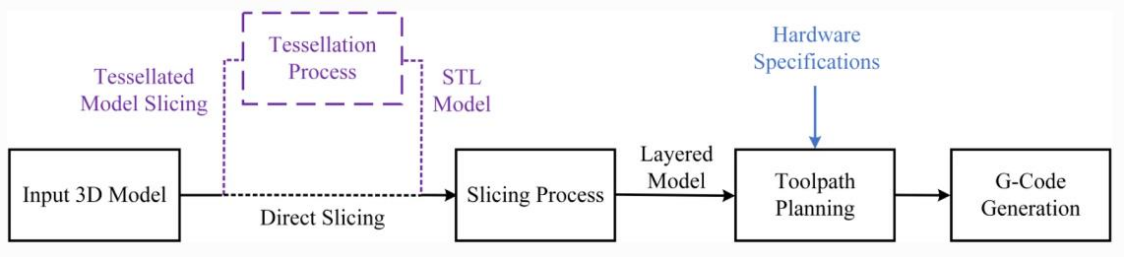

Figure 3. A general workflow in AM software processing [19].

The main function of the slicing software is to cut the model into several layers, analyze the closed path and convert it into commands for 3D printers. For only one slicing step, it used to take hours to slice, but at present the slicing process takes only a few seconds. Path generation software is intended for additive manufacturing and the dedicated software generates paths at a fast speed [20]. Control commands applicable to the additive manufacturing machine are generated and executed based on a two-dimensional profile.

Based on standardized methods, robots for 3D printing can achieve the functionality of 3D printers by adapting to the machine programming languages of diverse robot manufacturers. For instance, Werner et al. proposed a software solution called MeshSlicer [21]. In that research project, the customized fused-filament-fabrication (FFF) print head was connected to an Asea Brown Boveri (ABB) six-axis machine. The G-code output by the conventional slicer reflects the 3D model to be printed. Afterwards, the necessary modifications are executed so that G-code output can be imported into the next linked software in the manufacturing process. MeshSlicer integrates the corresponding code required for necessary steps. The MeshSlicer program quickly converts the G-code instruction into ABB code to adapt to the corresponding ABB machine motion language. In order to simplify these steps, the created program consists of a post processor as a main component, which processes the data and divides the data into two parts. These two parts are motion commands and extrusion values, so that industrial machines can produce models through additive manufacturing. In order to test the algorithm of MeshSlicer, several models, such as pyramids and cubes, were imported into the software. The information including edges and points of the 3D models can be extracted, and the complexity of the models varies. However, MeshSlicer cannot indicate the supporting materials that might be required. During the printing process, unoptimized path planning based on MeshSlicer may result in the model collapsing. The result in Figure 4 showed that the printing required additional support structures and the quality of the printed tip and edges was not sufficiently good.

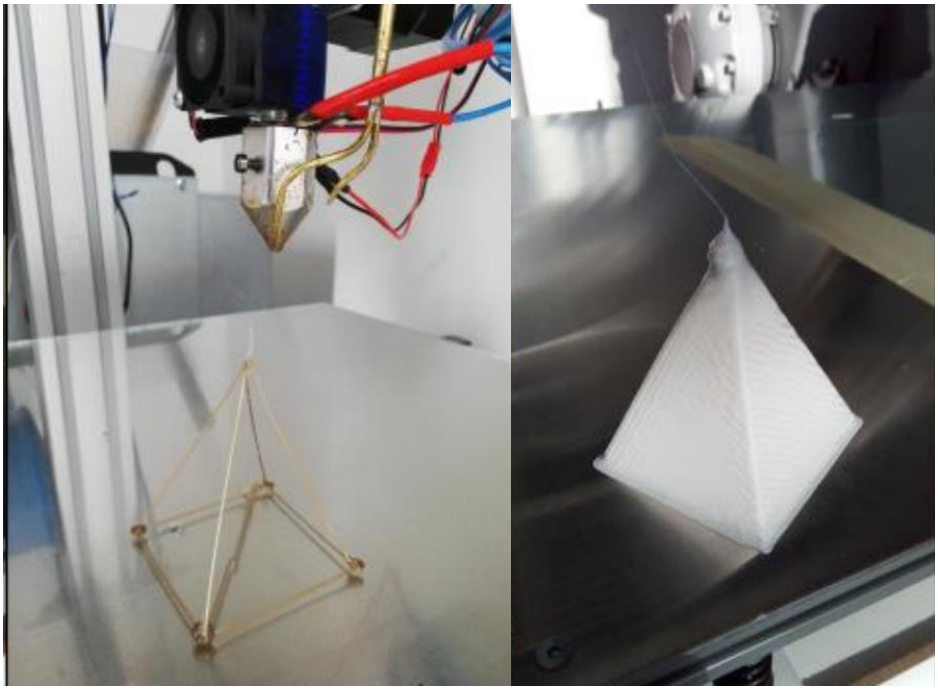

Figure 4. Printed object based on MeshSlicer [21].

Moreover, displaying images of printing paths in the software makes the printing process more intuitive. As shown in Figure 5, the path in two dimensions is displayed according to a given model. Therefore, the 3D representation of the deposition points of metal droplets can be displayed in the software development of the drop-on-demand 3D printing.

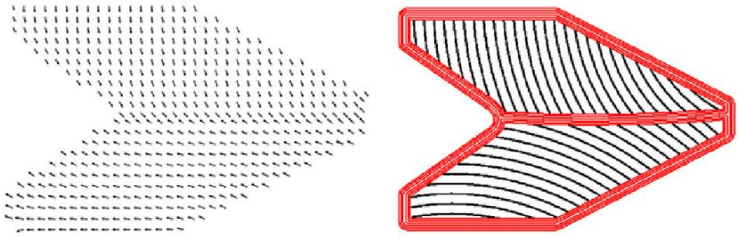

Figure 5. Printing path for a given model [22].

Widely used slicing software can be generated for printing path planning and filling. Open-source algorithms of slicing software can be selected, such as Slic3r or Cura Engine. Therefore, to apply to the metal-droplet printer in the project, a modification program for converting motion instructions based on slicing software is a suitable choice [23]. As mentioned above, in the research project by Werner et al., one processing software was written for ABB machines only. In order

to match a wider range of industrial machines from various manufacturers, a simplified and adaptable processing method for industrial CNC (Computer numerical control) systems can be developed.

1.2 Project situation and focus

The future of metal droplet additive manufacturing will be the direct printing of integrated parts, with high surface quality requirements [24]. The surface of printed layers based on metal droplets with high melting points is uneven, such as aluminum droplets in Figure 6, which to some extent hinders the internal filling of three-dimensional curved objects. In order to reduce surface height variation and roughness, exploring appropriate strategies to fabricate curved shapes with internal filling remains an important topic to be addressed.

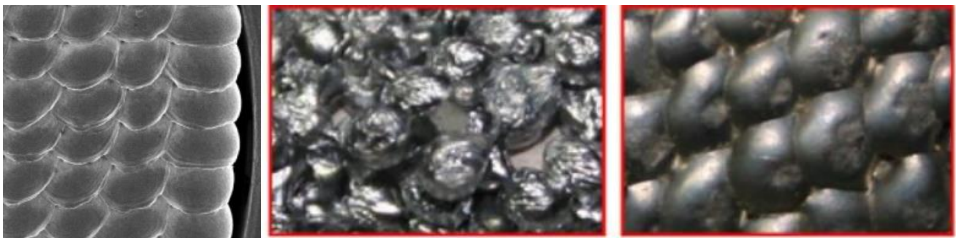

Figure 6. Samples manufactured by depositing metal droplets [25], [26].

Based on the literature review, there is a lack of sufficient studies in terms of the path planning for printing curved shapes with metal droplets. Different from the straight-line deposition, printing paths involving curved shapes are with multiple arcs. In additive printing, target objects, such as cylinders and hemispheres, are sliced into layers. In this manner, three-dimensional curved objects can be transformed, with each layer being analysed in a two-dimensional plane. Based on the curvature, that is the variation rate of the arc direction as regards the arc length, the printed contour of curved shapes is a closed flowing line in each layer. Aiming to improve the deposition, the presented study provides an optimized approach to

manufacturing curved shapes, involving the position generation of print path points and the motion control. The deposition control over the manufacturing of curved objects is achieved by the method, called adaptive droplet-spacing with angular displacement.

Additive manufacturing of metals with a high melting point is investigated based on an extruder with induction heating. Since the radius of a single metal droplet is on the millimeter scale, a number of metal droplets are required for the fabrication of small-sized parts. The proposed solution can be applied to droplet-based techniques for rapid prototyping, and hence the broad scope is beyond metal droplets. In terms of the drop-on-demand technique, the optimized printing path strategy is proposed to improve the layer flatness and the printed contour accuracy of curved shapes, taking into account the filling material consumption. Additionally, efforts are made to integrate printing system components in metal additive manufacturing, and therefore the system operation can be supported in the compatible software and hardware.

In the project, the objectives are as follows:

1) The project aims to optimize the droplet-spacing to adapt to various curvatures, achieving a reasonable number of droplets for filling curved shapes internally without visible voids.

2) In the software processing of the deposition paths, a software program can be designed to simplify the operational steps in additive manufacturing.
3) Dynamic changes in droplet energy and deposition radius at different release heights can be obtained, as a basis for spacing of neighboring droplets in the practical path planning.
4) The optimized drop-on-demand path-planning strategies are adopted to print two-dimensional curved patterns, and three-dimensional curved objects can be completely filled and fabricated. Based on the proposed strategies, the printed surface quality can be superior compared to general methods.

1.3 Thesis structure

This thesis is set up as follows.

In chapter 1, the research background is introduced, and the objectives are included. A literature review on the research topic is presented in chapter 2.

Chapter 3 presents the details of the experimental system with experimental methodology, and describes the methods to support the system operation.

In chapter 4, the optimized deposition path strategies, the analysis of the droplet deposition, and the printing of curved shapes are presented and discussed.

Chapter 5 draws a conclusion and states the future outlook to improve the manufacturing quality.

Chapter 2 Literature review

2.1 Path planning

2.1.1 Continuous printing path

The development of continuous printing path is mainly for fused deposition modelling or other continuous manufacturing techniques. For printing simple patterns, such as quadrilaterals, there are generally direction-parallel methods, including raster or zigzag [27], [28]. Based on continuous extrusion, the travelling path was improved to achieve no retraction [29]. Since additive manufacturing requires the printing of multiple layers, Wei et al. used parallel printing for different layers in horizontal or vertical directions [30]. As shown in Figure 7, through optimization such as zoning, the cross shaped parts were manufactured [31], and the part was printed at different speeds in different colored areas in Figure 7 (i). The zoning optimization reduced visible hole defects.

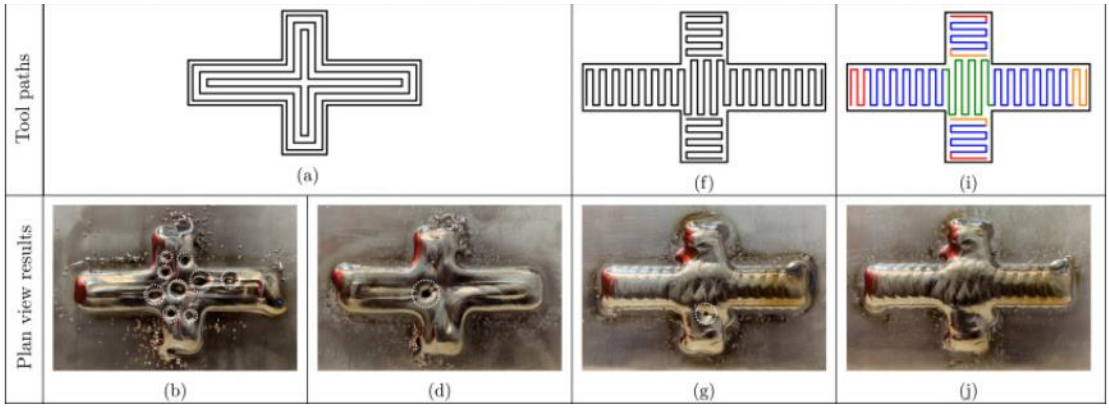

Figure 7. Cross shaped components [31].

Another common continuous printing strategy is contour-parallel manufacturing, which can reduce the appearance of sharp corners [32], [33]. For thin-walled structures, the contour-parallel manufacturing has been adopted in order to approximate the structure [34], [35]. In directed energy deposition, similar to the paths in Figure 8, the zigzag filling and the contour-parallel filling were generated by Biegler et al. [36]. In addition, deposition lines of different thicknesses were produced to form continuous paths without gaps [37].

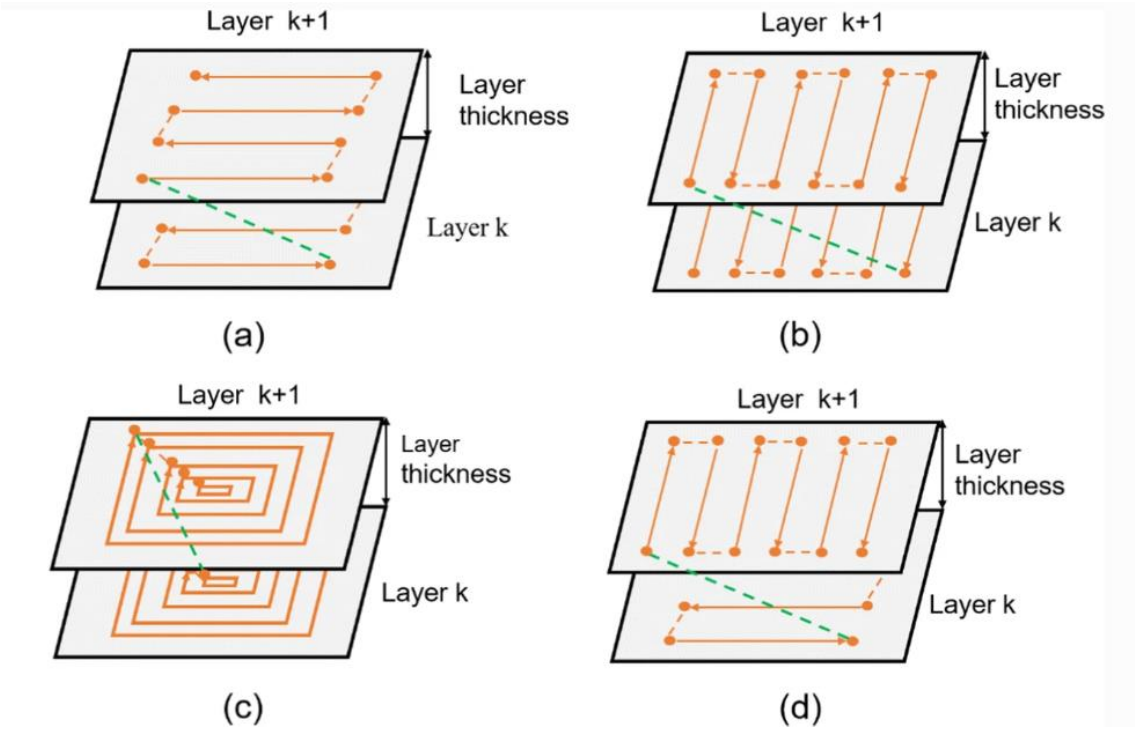

Figure 8. (a) Zigzag along X axis, (b) zigzag along Y axis, (c) contour-parallel, (d) zigzag along X axis, Y axis [30].

Fang et al. [38] mentioned and compared the contour-parallel paths and Hilbert curves for various printed regions, as shown in Figure 9. Moreover, a spiral continuous path was proposed by Ren et al. [39]. However, the spiral continuous path requires a constantly changing width of the deposited line, which does not apply to droplets with constant size.

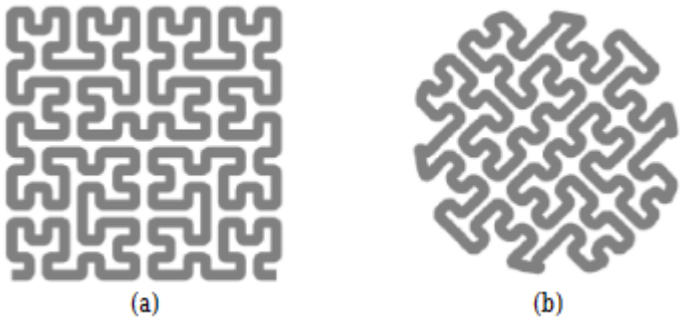

Figure 9. Hilbert curves for (a) square (b) circular shape [38].

As shown in Figure 9 (b), regarding the circular shape, continuous printing may cause the printed edge to differ from the ideal contour. When corners are present in the printing path, the continuous deposition cannot be controlled effectively to minimize the overfilled field at the corners, which results in an uneven printed object, as shown in Figure 10.

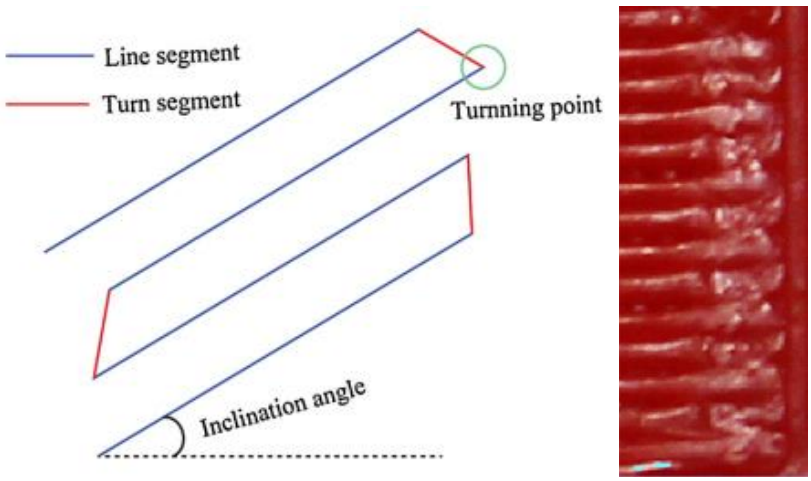

Figure 10. (a) Continuous deposition path with corners (b) continuous printing result [40].

2.1.2 Drop-on-demand printing

Different from the continuous printing, the on-demand printing is highly controllable, and it has the potential to yield more uniform parts. As shown in Figure 11, the on-demand deposition, represented by the circles, allows for effective control of the droplet landing points. This reduces the overfilling to some extent, leading to a flatter surface of the printed object based on the drop-on-demand technique.

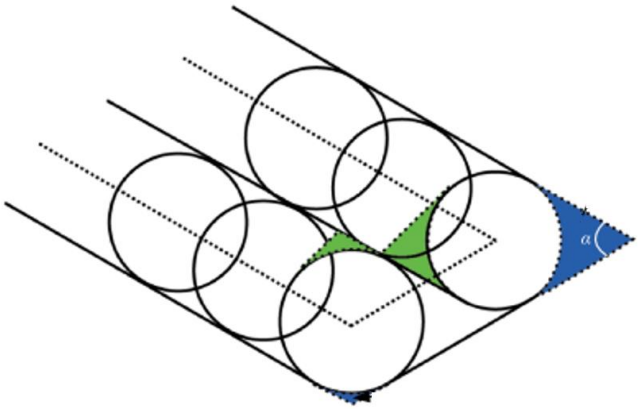

Figure 11. Deposition pattern at corners [41].

As droplets are created and deposited on the area to be printed, excessive material in overfilled areas is minimized. Therefore, the on-demand printing has a higher material usage rate than the normal continuous jetting, which reduces the material waste. In terms of the power consumption in heating materials for printing, droplet-based techniques basically do not involve electron beams or lasers, saving the costly expense of the equipment associated with lasers and beams. In SLM-based additive manufacturing, single-mode lasers are used as a heat source to melt the area within 20 cm^3 per hour, consuming the power around 1000W [42]. Moreover, the power consumed is greater than the output power, and the output using electron beams is higher than 2000W for melting areas within 80 cm^3 per hour [43]. Regarding droplet-on-demand technology, the related machine produces droplets intermittently, which also lowers the power consumption in operation compared to the continuous printing. Therefore, droplet-based techniques set the stage for cost-effective manufacturing due to relative low energy input and cost. In addition, droplet sizes of 1mm or even 0.1mm are suitable for small sized manufactured parts, and the generation of smaller sized droplets can further improve the uniformity of manufactured objects.

Cheng et al. [44] generated low melting point tin droplets, and the tin droplets were deposited separately on a table stage. However, the table stage had only two directions (X and Y directions), and three-dimensional objects were not constructed. Fang et al. investigated the temperature effect of droplet and substrate on the deposition of tin droplets in the process of forming thin-walled objects [45]. Yamaguchi et al. printed three-dimensional structures according to the desired

droplet landing position [46]. Cao and Miyamoto [47] printed square shaped container via aluminum alloys, based on a raster deposition path, as shown in Figure 12.

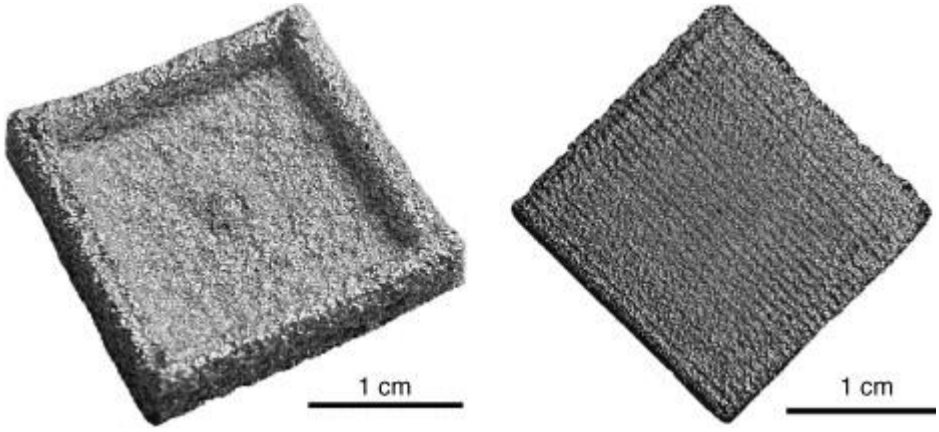

Figure 12. Square shaped part via a raster deposition pattern [47].

As the printed shapes transition from lines to polygons, conventional raster or contour filling patterns are not suitable for printing precise peripheral contours without voids. In the linear printing, the length between two centers of adjacent droplets was further studied to achieve better printing geometric quality. The short lines composed of droplets can be divided into four types: a broken line, a partially connected line, an ideal connected line, and protrusion caused by excessive overlap. When the spacing between two neighboring droplets is greater than the droplet deposition diameter, there is no physical connection among neighboring droplets, and hence a broken line is formed in Figure 13 (a). Due to the error in the droplet landing position, neighboring droplets may be in contact, which composes a partially connected line in Figure 13 (b) under critical spacing conditions. Therefore, the distance between two adjacent droplets should be less than the droplet deposition diameter based on the drop-on-demand technique. When the spacing between two adjacent droplets is around the ideal distance for the horizontal line deposition, as shown in Figure 13 (c), the straight line is uniform and the line width remains basically the same, except for the two ends.

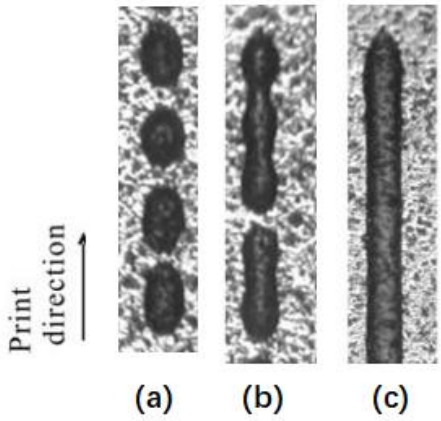

Figure 13. (a) A broken line, (b) a partially connected line, (c) an ideal connected line [48].

In addition, excessive overlap causes another situation, particularly obvious for metal droplets. As shown in Figure 14, wavy lines or protrusion are presented when the droplet spacing is less than the lower limit of the ideal distance range for the horizontal line deposition.

(a)

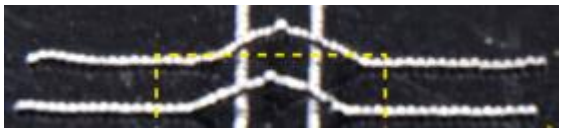

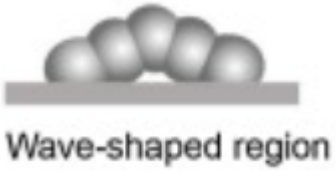

(b) (c)

Figure 14. (a) Deposition morphology [12], (b) wavy lines [49], (c) schematic [12].

Various overlapping extent of molten wax droplets have been studied for the formation of straight lines, and the critical relationship of line breakage has been explained [48]. In addition, the diffusion length of the dropping water droplet

combined with the previous water droplet on the steel surface was analyzed [50]. Different combinations were listed based on the relationship between diffusion length and ideal length. Two-dimensional straight lines and squares were formed using 87 wt% glycerin-in-water droplets by Dalili et al. [51]. Exceeding the range of overlap ratios led to breakage or irregular shapes.

Since the deposition unit of the metal-droplet printing is an independent metal droplet, the workpiece surface will form a "shell" shaped and uneven morphology, as shown in Figure 15.

Figure 15. Deposited lines [52].

Two-dimensional patterns can be printed by the horizontal movement of the nozzle or deposition substrate. When the spacing between droplets is greater than the droplet deposition diameter in top view, there is no physical connection among neighboring droplets. Based on various travelling speeds and droplet sizes, continuous and discontinuous lines were printed, as shown in Figure 16.

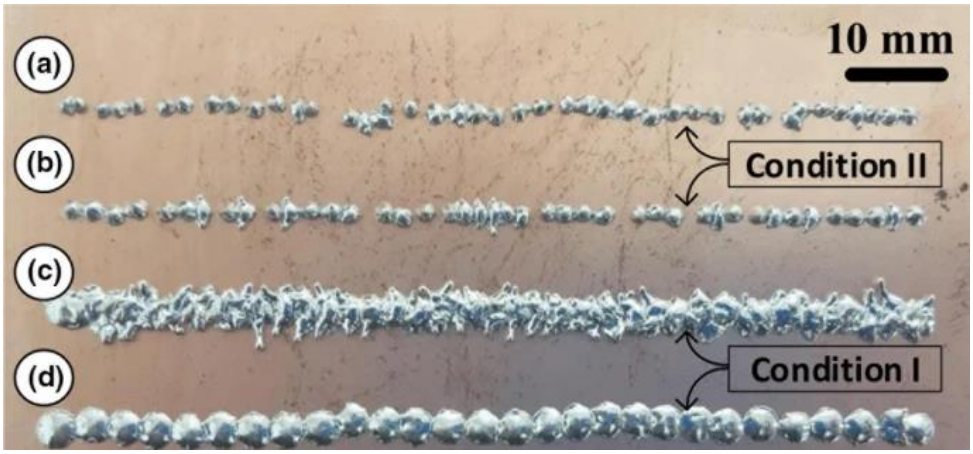

Figure 16. Continuous and discontinuous lines [53].

Qi et al. [52] predicted the ideal spacing of metal droplets by analyzing optimal overlapping in straight lines.

$$w_x = \frac{4\pi R_i}{3\sqrt[3]{\left(\frac{4}{(cos\theta+2)(1-cos\theta)^2}\right)^2 \times (\theta - sin\theta cos\theta)}} \quad \text{Equation 1}$$

where w_x is the droplet spacing in the straight lines, R_i is droplet radius and θ is solidification angle. Qi et al. [52] utilized Sn60–Pb40 alloy as droplet materials, and copperplate as deposition substrate platform. Sample parts were manufactured with a pneumatic metal-droplet generator, and droplet spacing results in various metal-droplet overlap and bonding strength. Thus, different longitudinal and transverse droplet intervals were tested at a substrate temperature of 90 °C with a droplet temperature of 270 °C. Parameters such as droplet generation frequency and spacing were adjusted to reduce porosity. The printing with a small spacing made the overlap ratio high, which may cause protrusions and holes, as shown in Figure 17.

Figure 17. Deposited layer with a small spacing [52].

Utilizing the metal printing materials Sn63%Pb37% and AlSi12, Zhang et al. [49] studied the relationship between linear droplet-spacing and depositional morphology, demonstrating a variety of depositional shapes involving diagonal, wavy lines. Dou et al. illustrated mechanism of the spread and retraction errors, and they used a model to predict the position of two metal Sn-40 wt.% Pb droplets [54]. Additively manufactured stacking in the vertical direction can form three-dimensional shapes. In terms of metals with high melting points, Fang et al. [55] printed columns using aluminum alloys, as shown in Figure 18 (a). The vertical deposition is not a straight line perpendicular to the horizontal plane due to droplet landing deflection. Three vertical columns with different droplet numbers were formed with heights of 0.5 mm, 2 mm and 5 mm as shown in Figure 18 (b) [56].

The effect of the deposition deflection became significant as the number of deposited layers increased.

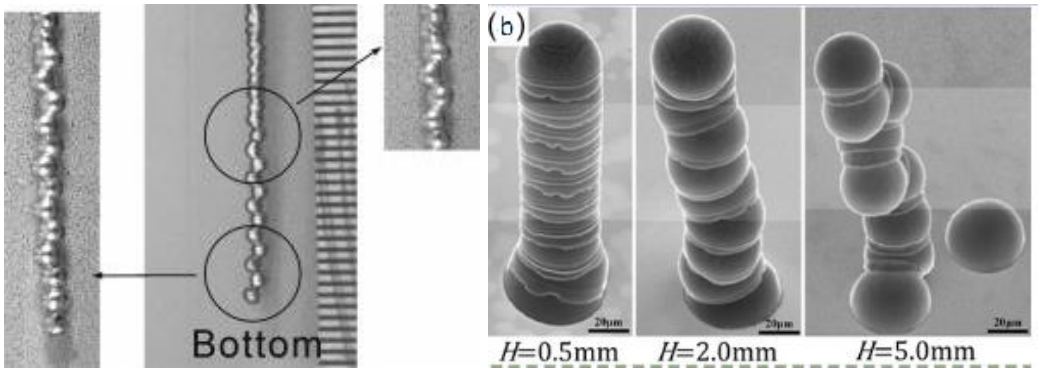

Figure 18. (a) Printed vertical column [55] (b) columns with different droplet numbers [56].

According to the distance between each two droplet centers, polygonal structures can be additively fabricated with droplets. Inconel alloy 600 was used to fabricate simple objects by 3D Micro welding [57]. The rearrangement of the droplets deviated from the desired contour, resulting in a greater dimensional error between the fabricated object and the desired object. Zhang et al. [58] conducted experiments on the printing of thin-walled triangular contours with single-droplet thickness. They used the metal droplet temperature of 573 K and substrate temperature of roughly 295 K. The trigger of piezoelectric ceramics causes the bars to vibrate in liquid metal, which pushed metal droplets out of the nozzle. After manufacturing, the height difference between the starting and ending droplets on the closed profile reflects the degree of overlap. In the study, the droplet spacing around the corners was optimized in order to reduce the excessive overlap around the closed corners, as shown in Figure 19. However, the spacing of the droplet bonding for the internal filling was not analyzed.

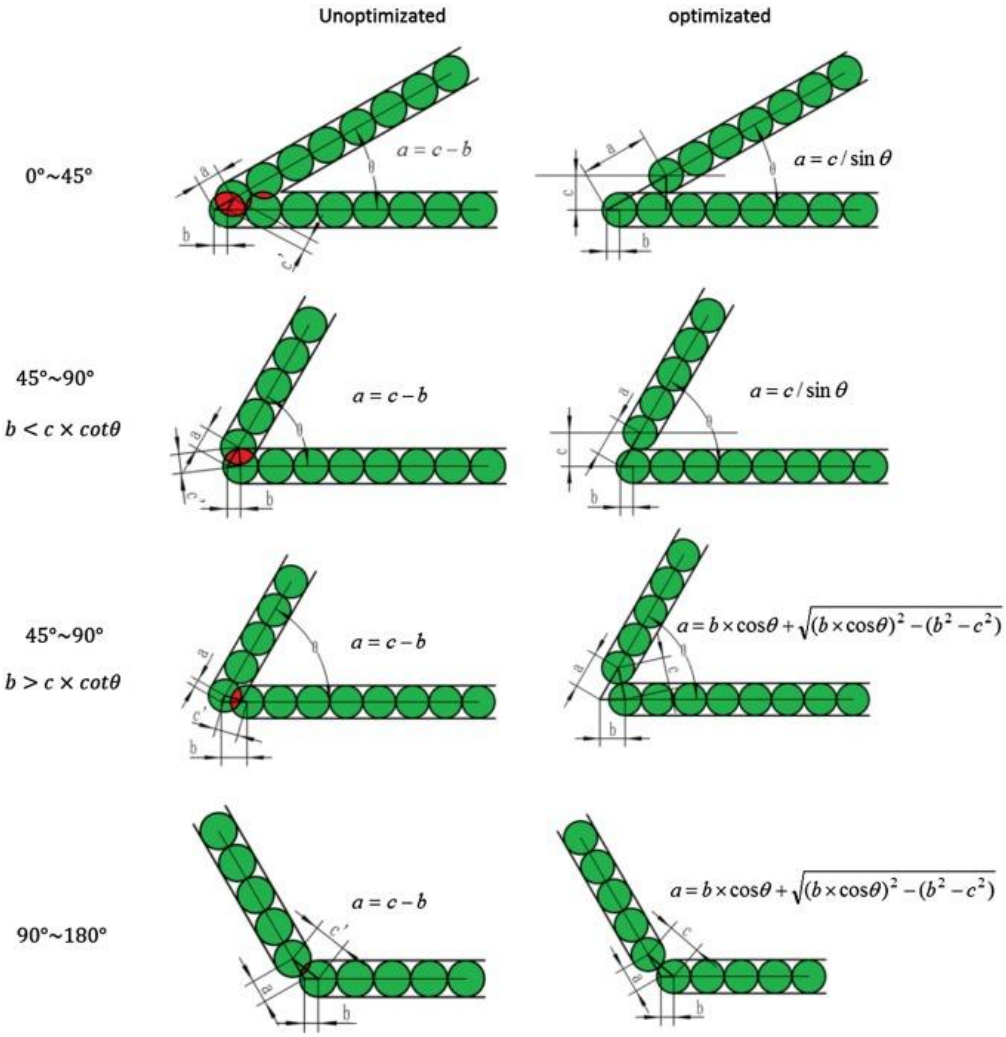

Figure 19. Droplet position at corners [58].

Dou et al. [59] discussed spacing offsets to manufacture triangular shaped objects with the internal filling. However, the droplet spacing in one line and the line spacing between adjacent line segments should be varied for various shapes accordingly, since the droplets and the line segments are of different sizes. As a result of this, the spacing offset for the internal filling needs to be further optimized. In addition, the cross-sectional profile printed by Dou et al. is triangular contours, a combination of straight-line segments. They approximated arc segments as straight lines, and the droplet overlap on the curves has not been studied.

2.2 Dimensional accuracy and roughness

Extrusion-based printing involves continuous and drop-on-demand manufacturing. Currently, there are some challenges in the printing, including low printed contour accuracy, and excessive surface roughness caused by its own technology and process parameters [60]. The process parameters contain orientation of 3D printing, filling pattern, printing speed, and so forth [61]. Various contour shapes were printed based on the continuous printing [62], and dimensional accuracy varies depending on the shape of the part being manufactured. Deswal et al. compared different models to set process parameters based on the continuous printing with the aim of improving the contour accuracy of fabrication [63]. Based on two materials (Nylon and ABS), the manufacturing parameters were varied to achieve output dimensions at high quality respectively [64].

Surface quality is also a concern in additive manufacturing, and parts with low surface roughness improve properties such as fatigue resistance [65]. Furthermore, surface quality has a considerable impact on the cost and efficiency of the overall manufacturing process [66]. Ahn et al. analysed the effect of different deposition directions on the surface quality based on the raster printing path [67], as shown in Figure 20. In order to reduce the roughness of the additively printed outer contour, the optimal manufacturing orientation of the printed parts was obtained by a genetic algorithm [67].

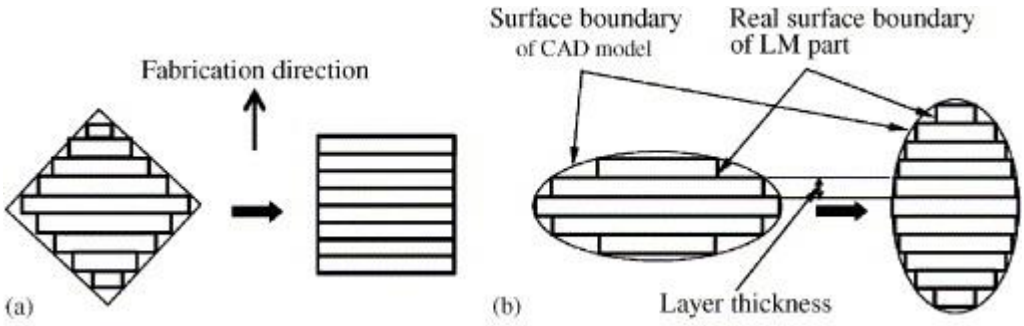

Figure 20. Different deposition directions for (a) square, (b)curved shapes [67].

Fahad et al. adjusted the continuous printing speed to fabricate an object from 35 to 55 mm per second [68]. The printing results showed that the flatness in the low-speed case was superior to the deposition at high speeds. Based on the

continuous printing, Bakar et al. considered the effect of the object shape on the error and flatness of the printed contour [69]. The result indicated that the fabricated cylinders have greater errors in size and surface roughness than the fabricated cubes. Due to the staircase effect caused by multi-layer printing, the fabricated surface quality of curved contours is worse than that of straight contours [70].

In the drop-on-demand inkjet printing, the shapes can be printed via TIFF files. Elkaseer et al. predicted droplet positions based on pixels in the TIFF files, and they investigated the effect of image resolution and droplet size on the formation in the printing [71]. The method proposed by Elkaseer et al. is pixel-based and therefore limited to two-dimensional predictions. In their study, based on a low resolution of 360 dpi, the size error of more than 27% was presented in the samples formed by larger droplets. With respect to drop-on-demand metal printing, thin-walled triangular contours with single-droplet thickness were fabricated based on the droplets of Sn63%Pb37% melted at less than 300 degrees [58]. By adjusting the droplet position at the triangular corners, the fabricated layer flatness was improved according to the height variation.

In terms of aluminum droplets similar to the material used in the project, Zhong et al. fabricated a tube with a square cross-section using the generator they designed, and the usability of their generator was verified to extrude the droplets [72]. However, the dimensions and roughness of the fabricated square profile were not examined or measured. In the study of Cao and Miyamoto, the square shaped containers consisted of aluminum droplets were printed based on a raster deposition path [47]. The length and width in the horizontal direction were measured and the dimensional error was around 6.3%.

According to the previously mentioned studies, various manufacturing parameters were considered, and the impact on the quality of the manufactured parts was evaluated. For different shapes, materials and manufacturing process conditions, the parameters need to be optimized to improve the ultimate quality of additive fabrication. However, insufficient attention has been paid to printing and filling curved shapes internally, utilizing the drop-on-demand technique.

Chapter 3 Experimental system and methodology

3.1 Metal additive manufacturing system

The metal additive manufacturing core system is shown in Figure 21, which involves a moving and deposition part (including a wire feeder and a 3-axis CNC linear motion platform), and a heating part (including a ceramic heating substrate and an induction heater). The connections in the two parts are presented in Figure 22 & Figure 23.

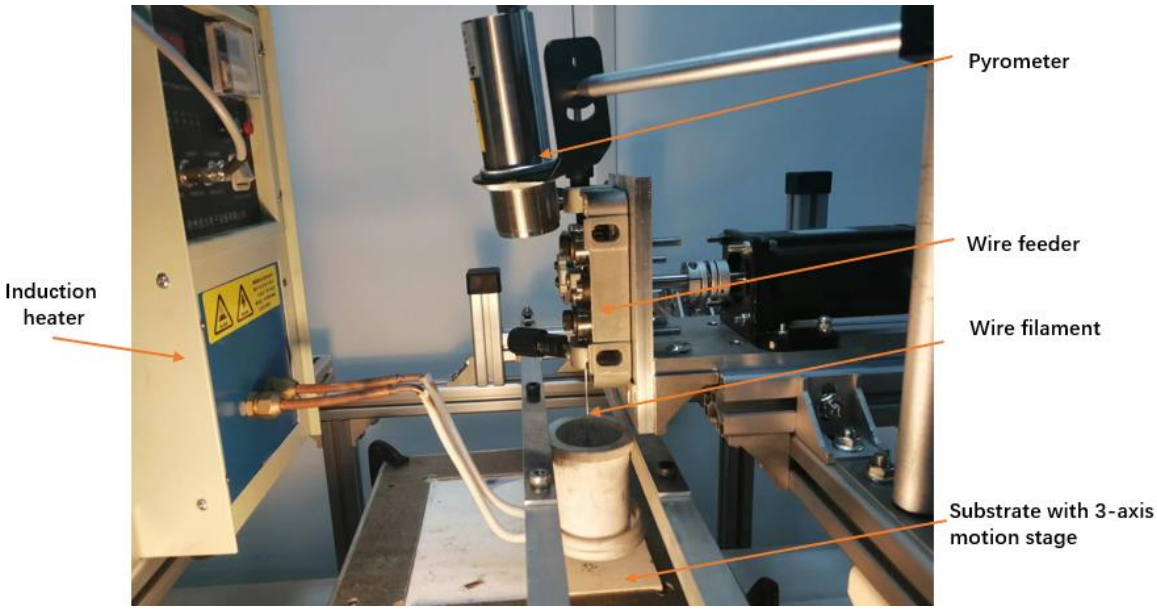

Figure 21. Core part of the metal additive manufacturing system.

By inductively heating the graphite to a temperature around 900°C (1173.15K), the tip of aluminum 6061 metal wires is melted as the wire feeder travels downwards allowing the wire tip to touch the graphite. The wire feeder retracts to create droplets, which can be produced in varying quantities as required. The three-axis motion stage supported the substrate and moved it in three dimensions according to the motion commands of the planned paths. The molten droplets were deposited on the heated ceramic substrate, and adjacent droplets were remelted and bonded for additive printing.

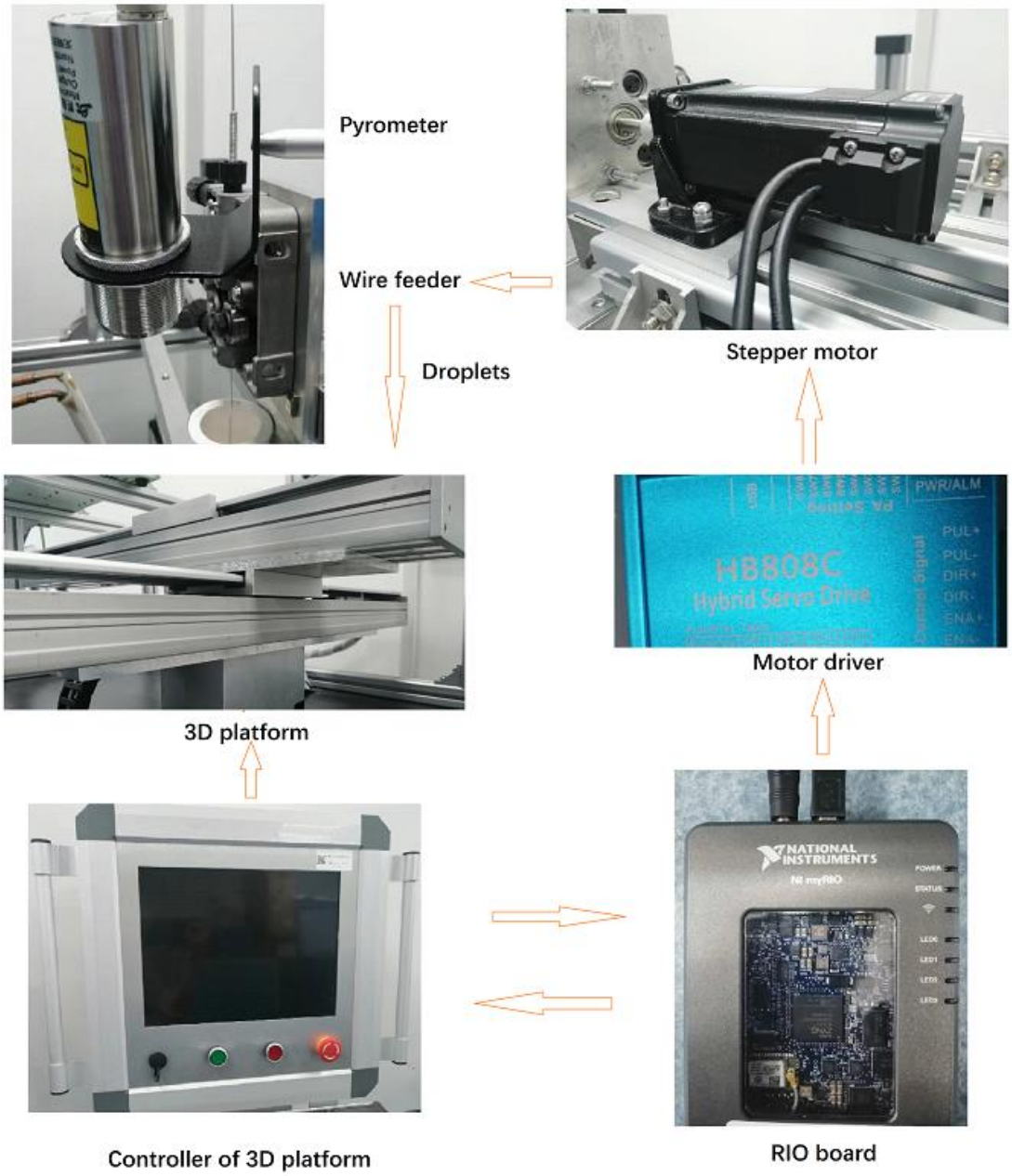

Figure 22. Moving and deposition part.

Prior to the 2022-23 research project, the experimental equipment did not work together in a complete system to print three-dimensional or even two-dimensional patterns. During this one academic-year-long project, the research as a master was conducted and the first version of the thesis was completed. More details prior to this 2022-23 project are as follows. Aluminum droplets were

generated by induction heating. However, there was no additional structure to support the induction heater on top of the 3D platform, and there was also no deposition plate that can be heated at a constant value. As a result, the generated droplets were dropped into a heat-resistant glass with water before this project.

In addition, no planned path points were created according to desired shapes. Therefore, the number of droplets as desired based on the drop-on-demand printing, and the droplet landing position on the heated substrate had not been tested experimentally prior to the project.

During the project, the integration work and preparation by the author are as follows, before testing the proposed path planning. Regarding the hardware integration, the induction heater and the PID controller were rewired and mounted in order to be placed on top of the 3D platform. The output power of the induction heater was adjusted by setting the parameters of the PID controller to achieve stable heating. Moreover, a shaft, which is the connecting part in the wire feeder, was redesigned for more stable droplet generation. The pyrometer and the stepper motor with the newly designed shaft were also fixed in an appropriate position to realize the closed loop printing control. Therefore, the change before and after the project regarding the hardware is similar to the consolidation process from discrete parts to the whole system as shown in Figure 21. With regard to the software preparation work, the code to control the wire feeder was modified and the travelling parameters were determined. The motion function suitable for on-demand printing was achieved and implemented based on the 3-axis motion platform. In addition, regular printing paths were generated by importing the drawn shapes into Ultimaker Cura slicing software. Relevant content on the software control is presented in the section 3.2 & 3.3.

Figure 23. Heating part.

In Table 1-3, more details can be seen in this study.

Table 1. Details of the induction heater.

Rated power	Rated power	Maximum output frequency	Heat conversion efficiency
15kW	15kW	100kHz	≥95%

When the heating area covered the area of the copper coil with a diameter of 6 cm, the graphite temperature was raised from room temperature to the set temperature within 1 minute. Then a steady state of heating was achieved by regulating output power and switching between low and zero power. The time taken for the substrate heating was roughly 40 minutes to increase the substrate temperature to the set temperature.

Table 2. Details of the infrared pyrometer.

Measurement range	Output	Wavelength	Emissivity
0-1200 °C	4-20 mA	1 μm	0.73 (for graphite)

As shown in Table 3, the diameter of the wire was chosen as 1.6mm since thinner wires were prone to bending, which is not conducive to the generation of droplets. Additionally, thicker wires easily destroyed the graphite outlet.

Table 3. Experimental conditions in the study.

Parameters	Values
Aluminum wire diameter d_{wire}	1.6 mm
Graphite outlet diameter	0.5 mm
Substrate temperature	385-400 °C
Graphite temperature	900 ± 10 °C
Droplet release height H	0.01, 0.02, 0.03 m

In order to produce small droplets, the graphite outlet diameter is 0.5 mm, as shown in Figure 24.

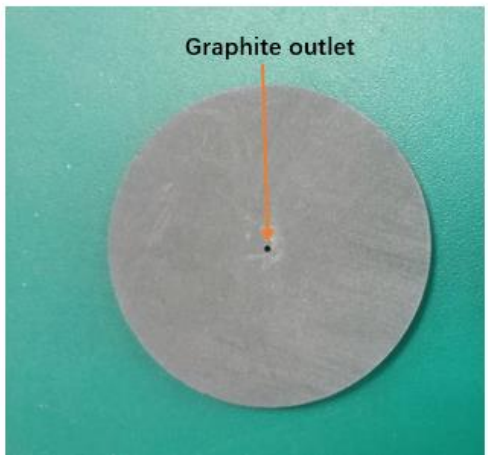

Figure 24. Graphite outlet.

The temperature variation of the substrate platform came from the heating source underneath the platform, so that the actual heating temperature in the center of the platform was slightly lower than the displayed temperature. It was difficult to increase the substrate temperature above 400 degrees, since the heating power of the substrate was basically equal to the heat dissipation over 400 degrees. The droplets were released from the graphite outlet, and hence the droplet release height includes the thickness of the crucible bottom, as shown in Figure 25.

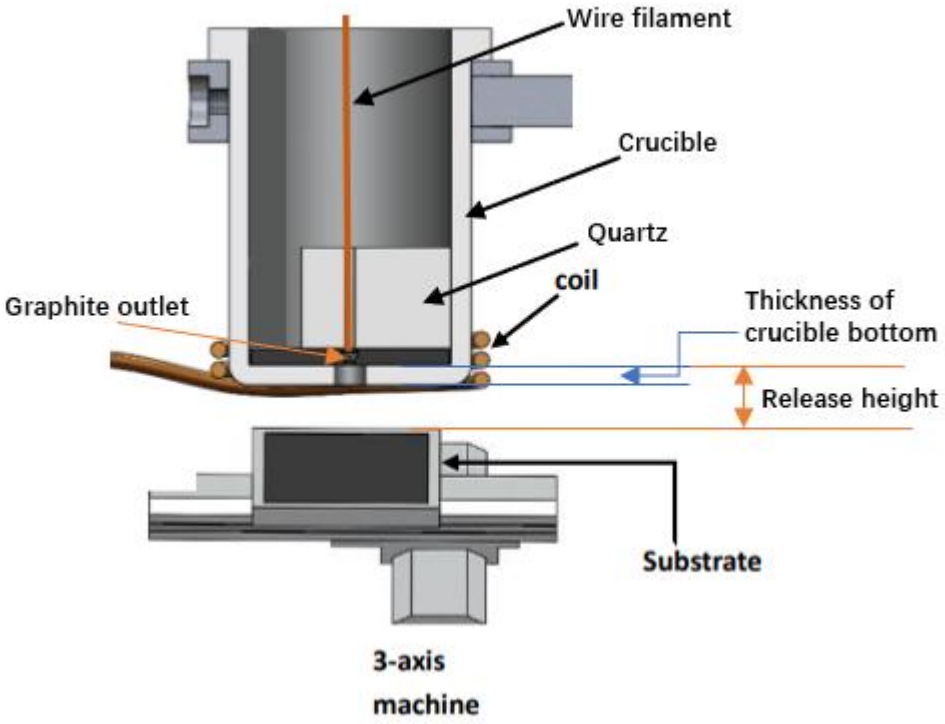

Figure 25. Schematic of the droplet release height.

To obtain the droplet extrusion, preliminary experiments of the wire feeder motor were conducted to determine the parameters, as shown in Table 4. Droplets were created by the rapid travels of the wire feeder including descending and ascending.

Table 4. Employed parameters for the wire feeder in the trials.

Parameters	Values
Descending distance d_{sd}	10 steps (2.41 mm)
Ascending distance d_{su}	6 steps (1.45 mm)
Descending speed v_{sd}	0.45 m/s
Ascending speed v_{su}	7.5 m/s
Pause between droplets	1s

In the wire feeder, a HB808C hybrid drive was used to connect and match the 57HSE stepper motor. The shaft with the feeder motor was designed to fit the wire feeder structure, involving the groove positions, as shown in Figure 26. The steps for assembling the wire feeder are as follows. (a) The shaft was placed in the bearing, and the corresponding circlips were used to fix the shaft and the bearing. (b) The shaft part was connected to the coupler, and hence the wire feeder motor could move the wire filaments. (c) A key was placed in the shaft to prevent unnecessary movement. The gears for the size of 1.6 mm were placed, as a drive transition. Based on the design, the accuracy of the motor step angle was improved to produce droplets more stably.

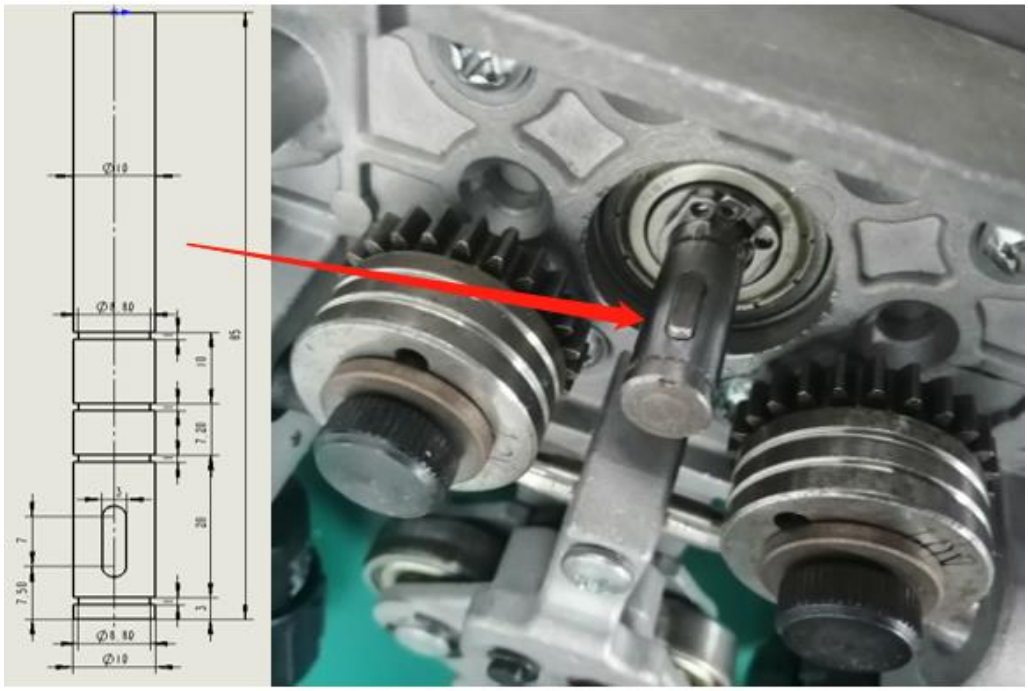

(a) (b)

Figure 26. (a) Shaft design (b) wire feeder assembly.

3.2 Software control

Software is an important component in determining the success of 3D printing. This is because the slicing software exports a collection of motion commands, which is the G-code. The motion commands contain the extrusion volume and other data for the extruder. For the CNC motion platform in the project, information such as the displacement path of the three axes was required, while other extrusion commands could not be executed. In addition, the paths of the metal-droplet on demand printing were not continuous, and hence the corresponding deposition points were required. The 3-axis motion platform stopped at each point, allowing metal droplets to fall onto the substrate. Manually modifying the G-code was basically impossible, as there were thousands or even tens of thousands of lines of the instructions. Therefore, an automated processing script was necessary. MATLAB R2022b was used since various functions are included in the MATLAB to meet the modification requirements.

The deposition paths in this project were generated point-trajectories for straight lines and curves in the drop-on-demand manufacturing. As shown in Figure 27, the flowchart shows the transformation of a continuous path into drop-on-demand points with the pause time.

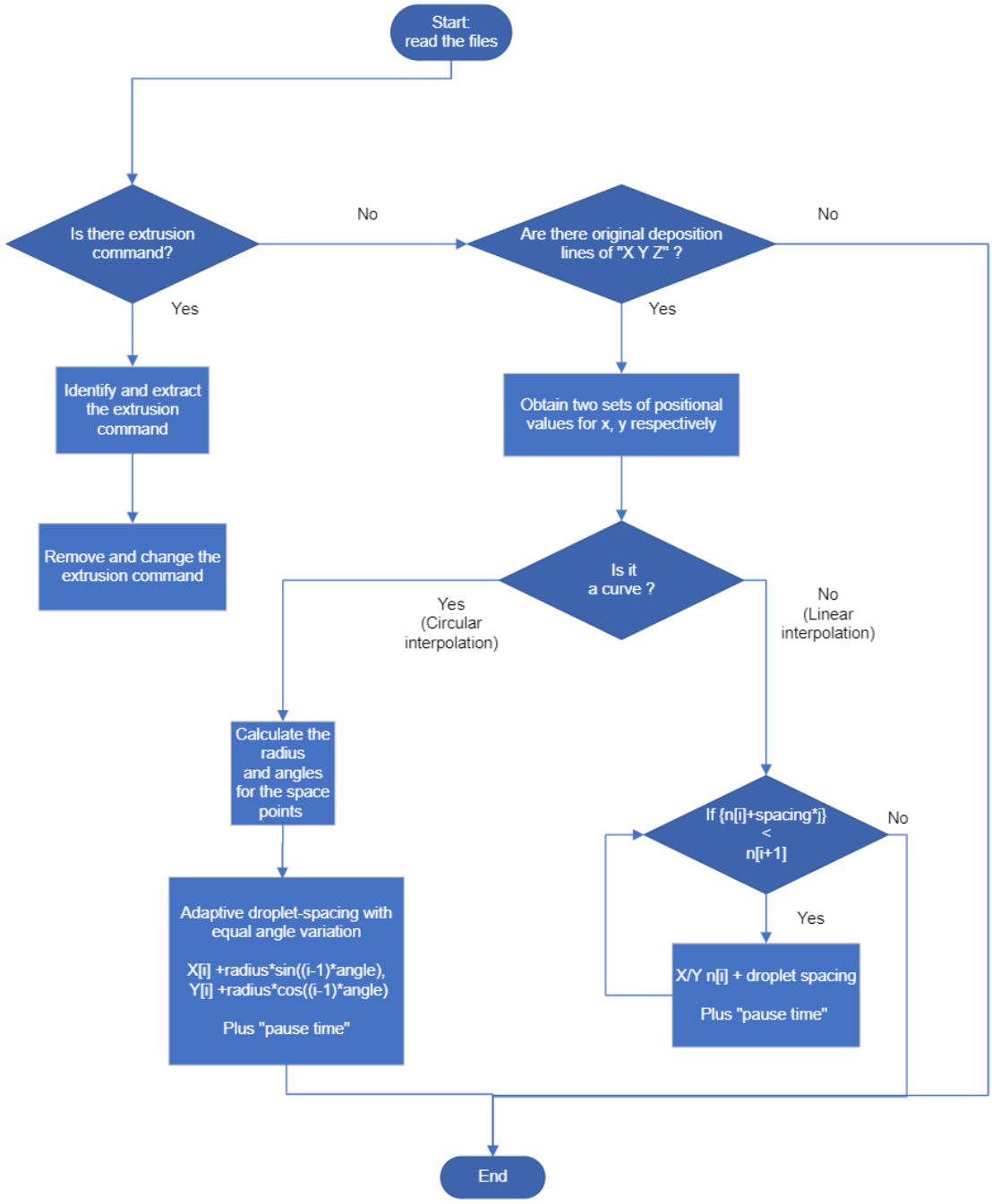

Figure 27. Flowchart of the deposition path transformation.

First step was to obtain the file where the original set of motion instructions G-code was located. In MATLAB, the “fopen” function was applied, which had two basic parameters. The first basic parameter is the full path where the document is located, and the second parameter sets whether to read or write. The function of ' r+' is to open the file to be read or written, while the function of 'w+' is to open or

create a new file to be read or written. If there is an existing file name and it is in the path of the first basic parameter, the original content of the existing file will be discarded. When the original document with motion commands was opened, the function to read a line was “fgetl”. It showed the next line without the newline character in the file. If the file is non-empty, a character vector will be returned. The code “while ~feof(gcommand)” was used to determine the last line of the document. The function of “feof” is to return the end-of-file indicator. The symbol “~” is the computation logic NOT, meaning that the while loop continues to the end of the file.

The function of “digitsPattern” is to create a pattern of digit matches. The variables in “digitsPattern” matched text consisting of exactly N numeric characters. The function of “wildcardPattern” is to create a pattern that matches as few characters as required, including zero characters. It extracts numbers and decimal points. The reason for not using this function is that “wildcardPattern” may recognize redundancy and cause command errors. In addition, the “replace” function can replace all occurrences of the substring with the newly modified string. The input text was a line of motion instructions, and the substring to be replaced was the extrusion amount, including the decimal point. The new substring was an empty string, which could be interpreted as a command to remove the extrusion command. The instruction for the extrusion was transmitted in another form to the controller of the wire feeder, thus allowing the motor to move or stop.

When the extrusion command was removed, the three Cartesian coordinates of the three axes needed to be read for the subsequent processing and the digital presentation in the 3D space. The data tested was with three decimal places before the decimal point, whereas in practice there were also four decimal places before the decimal point. Therefore, the number limit recognized by the program was modified to more decimal places. The function of “extract” is to return any substrings in the original data that match the specified pattern. If the original data is an array of strings or an array of character vectors, this function will extract the

substrings in each element of the original data. The three axes with corresponding values were each placed in their entirety into three different arrays, named NumX, NumY and NumZ. The digit matching pattern “digitsPattern” was used in order to extract the three values corresponding to the three axes. Finally, since all three values have a decimal point, the function of “str2double” is to convert all values of type string in the string array into an array containing double precision values, not scalars.

The original motion command has some repetitive elements. Generally, the “empty” travel motion command of G0 was executed first, followed by the original command of G1 carrying the extrusion command. The displacement information of the original G1 command as well as the previous G0 line of the “empty” travel motion command was important. This information was extracted to obtain the spatial displacement data before and after one point. In the project, the spatial displacement data was broken down into multi-line commands of droplet spacings to lay the basis for the drop-on-demand printing.

To determine whether it is G0 or G1 code, “strncmp” function was introduced to compare the first n characters between the two strings. Depending on the practical commands, the first 2 characters were compared to verify the preset conditions. If the current line is a G0 code-line, the tri-axis data for the “null” travel movement will be stored directly into the corresponding array. If the current line is a G1 code-line, a new event will be triggered. For the movements in the XY plane, the data of the X- and Y-axes in the previous and current rows were compared separately.

The curve paths were customized in the chapter 3, and the linear path planning was modified as follows. For instance, if there is no change in the X-axis position, the Y-axis position information will be required. The absolute value function of “abs” was used to ensure a positive difference between the Y-axis

values. According to the droplet size, the unit displacement was set, and the overall program divided a long straight line into a positive integer number (j) of points with the unit displacement. In the program loop, the Y-axis position will be added or subtracted by the unit displacement if the code line does not reach the line (j). If the Y-axis position in the previous row is greater than the Y-axis position in the current row, the subtraction code will be executed. On the contrary, if the Y-axis data in the previous row is smaller than the Y-axis data in the current row, the addition code module will be executed. The value in the last (j) line of the code is the position of the original G1 data. Similarly, when there was no change in the Y-axis position, the modification process was to swap the X and Y conditions in the judgement described above, as shown in Figure 28. Moreover, the parameter "P1" in Figure 28 (b) is the pause time.

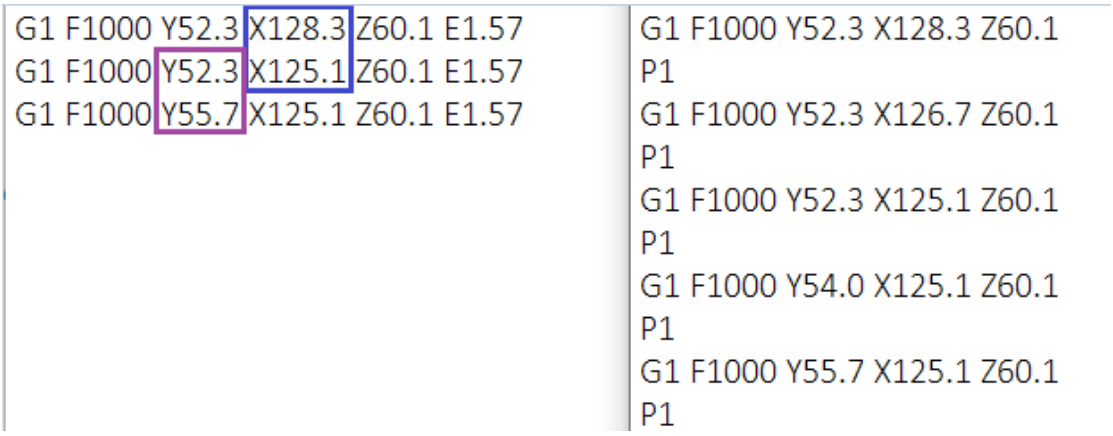

Figure 28. (a) Original, (b)modified commands.

It is worth noting that overwriting the data should be avoided. The original set of motion commands was saved to ensure that the original data was not lost, and hence the modified content was placed in a newly created file. The content of the modified 3D movements was written to the specified text file by "fprintf" function, which wrote all the elements of the array in order. In the project, the automatic modification program was designed for the CNC 3D control system, and hence the file format was converted for recognition.

The intelligent setting and modification of the designed program not only saves time, but also makes it easy to turn concepts into printed products. In order to display the spatial distribution of the deposition points, additional functions were implemented. As shown in Figure 29, in the simulation test, the deposition points for printing a cylinder are displayed as an example.

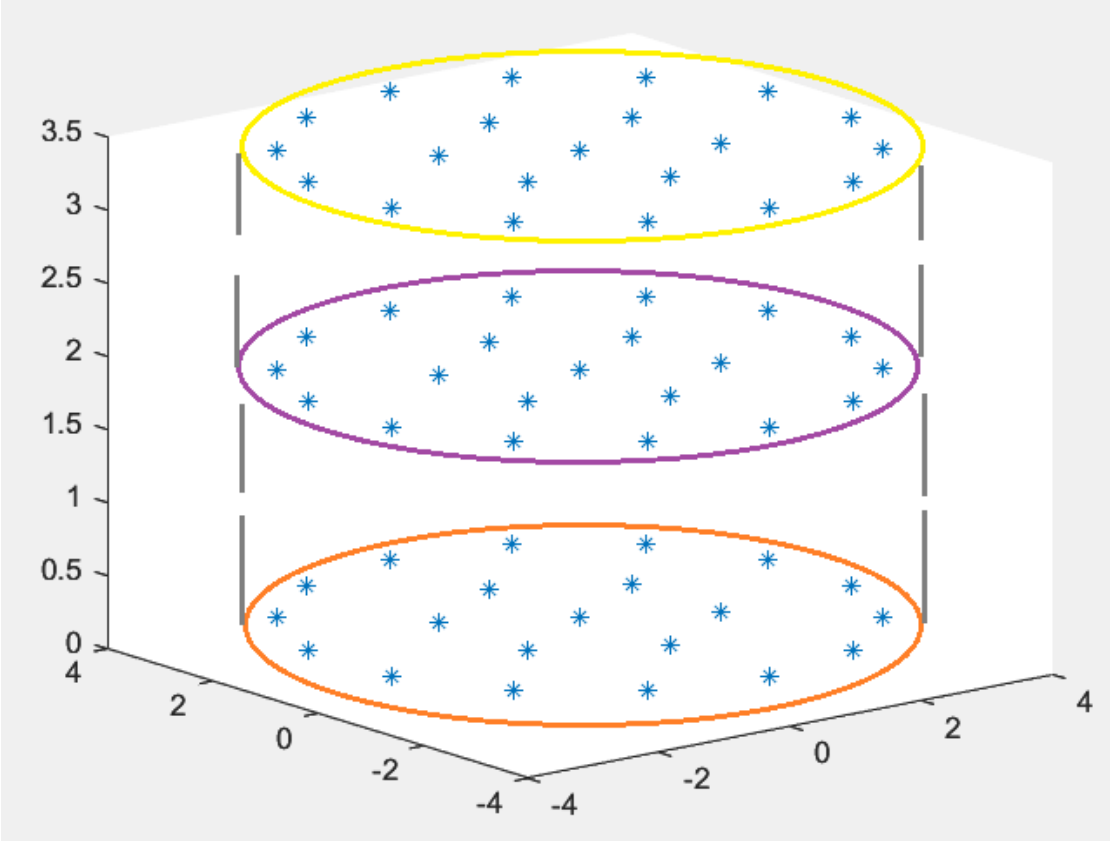

Figure 29. Example diagram of points for a cylinder.

The CNC system is based on Debian Linux. Generally speaking, Debian is more stable than Ubuntu as an Operating System suitable for servers. In addition, Debian as a whole has a very small base core and takes up little hard disk space and little memory. In addition, Xfce was used as the desktop in the CNC Linux system for the following reason. Xfce's terminal emulation is very powerful and, similar to

many other terminal emulation programs, allows multiple terminals to coexist in a single window. Since networking is available, additive printing can be controlled remotely. The Debian network configuration process includes configuring IP, gateway, DNS, etc. To realize networking, the alternative is to connect to a hot spot with a phone. Ultimately, G-code output was modified in the project, which could be adapted to the printing system.

3.3 Slicing and moving settings

Proper set-up and optimization in software are the foundation for successful additive manufacturing. Adjusting important and critical setup parameters can improve printing results. The parameters are modified depending on the different printing materials, the additive manufacturing requirements, etc. For parts with a small angle between the outer surface and the bottom horizontal plane, especially when the curvature is gentler, a larger layer height can produce more pronounced steps and layer textures. There are two strategies for solving this situation. The first strategy is to set a small layer height, and the second strategy is to directly change the position and angle of the parts in the slicing software. When adjusting the position of the model, the right click and the scroll wheel need to be used. The scroll wheel allows the image to be scaled and the model can be rotated by holding down the right button and moving the mouse. When the rotate icon is selected, two icons pop up, one for reset and one for flip. At the same time, a rotation guideline will appear on the model. The model can be rotated by moving the mouse along the guideline in the direction of the rotation.

The main purpose of filling is to support the internal structure. When the filled rate is too low or the filling is absent, the model tends to distort when the shell is being printed. If the filled rate is at a low level, there will also be a degree of warping created.

Due to the heaviness of the printhead assembly, the printer nozzle in the project was placed in a fixed position. The deposition heating plate was moved to the specified position in accordance with the transmitted motion command. When the deposition platform was in “an empty moving”, the filament consumables were not extruded by the nozzle. When the “idle” travel speed was too high, the instantaneous acceleration and deceleration were great, creating a large inertia that could easily lead to lost steps. Therefore, excessive “idle” travel speed was not used. Moreover, an acceleration and deceleration control can be applied to reduce acceleration. When moving from the current printed layer to the subsequent layer, there was a wide range of diagonal lines, that means a large displacement. The parameter "Z joint alignment" in the slicing was modified, and the beginning of the path in the layers was adjusted.

Regarding the control of the wire feeder, a designed program controlled the motor in the wire feeder, similar to the program developed by Gong and He [73]. The upward and downward travel of the wire feeder was determined by the rotation direction of the motor. The clockwise and anti-clockwise rotation of the motor was based on the transmitted signals from the NI myRIO board, which was controlled by the LabVIEW modules and the program.

NI myRIO is with an internal Xilinx Zynq chip, as an embedded system platform. There are two main modes on the RIO target, one for Real-Time scanning and the other for Field Programmable Gate Array (FPGA) mode. The logic functions of the FPGA can be utilized through the integrated modules of LabVIEW. Using an oscilloscope, the signals of the Input/Output (I/O) interface on the NI myRIO target were measured and displayed. The real time scanning mode has varying signal trigger intervals, and hence the moving time of the wire feeder could not be determined. In order to control the motor more precisely, the program in the FPGA mode was developed in the project, which allowed the signal generation

time to be determined. A user interface was created for setting the parameters of the wire feeder, as shown in Figure 30.

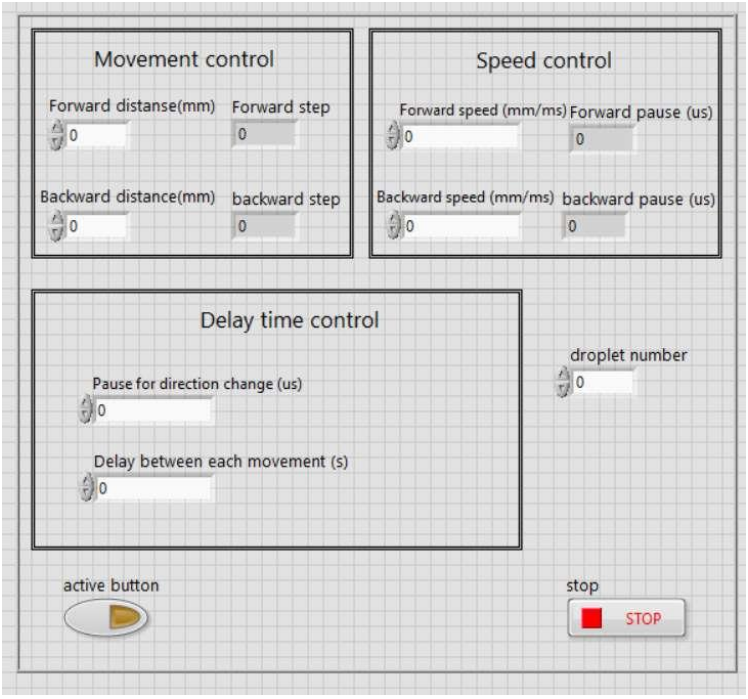

Figure 30. User interface for the wire feeder.

"Forward distance" represents descending distance d_{sd}, which was determined by the "forward step" of the stepper motor. "Backward distance" represents ascending distance d_{su}, and the movement speed was based on the pause time.

With appropriate settings, the software and hardware in the metal additive manufacturing system could support the additive printing in three dimensions.

3.4 Deposition for printing

Depending on the desired release height, the distance between the three-axis stage and the bottom of the crucible in the Z-axis direction was adjusted. As shown in Figure 31, the release height is the sum of two segments, the thickness of the crucible bottom and the distance from the crucible bottom to the substrate.

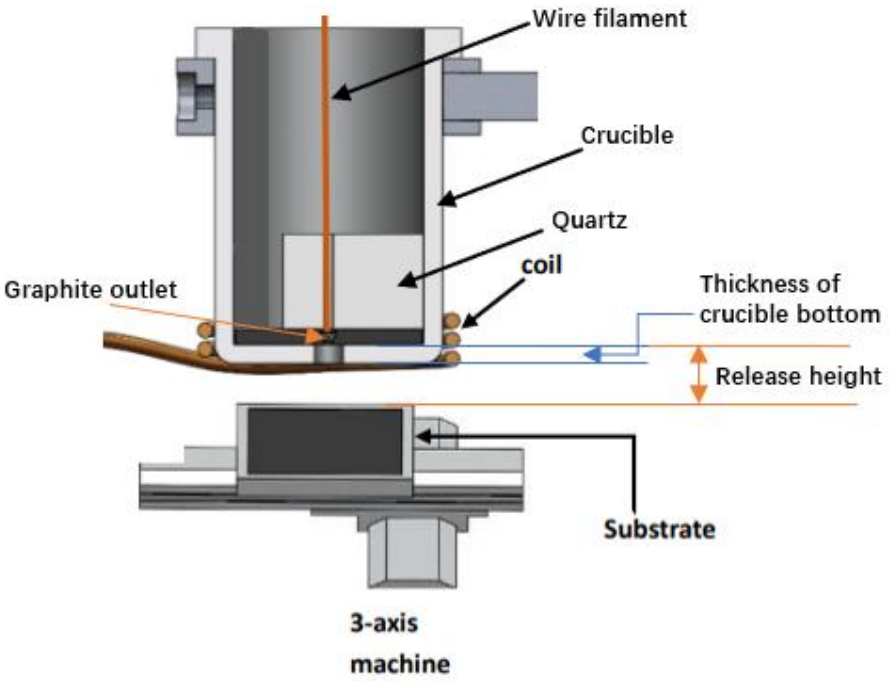

Figure 31. Schematic of the droplet release height.

The thickness of the crucible bottom is approximately 6 mm, and the vertical distance from the three-axis stage to the crucible bottom was measured to be 80 mm, after Z-axis zeroing. Therefore, for the release height of 1 cm, the three-axis stage was set and elevated to “+76mm” in the Z-axis. When the printing is in one layer, the Z-axis will be fixed in order for the stage to move in the X-Y plane. When the setup is complete, the metal additive manufacturing system can work as a whole to generate small droplets in a relatively stable manner. The above steps were repeated at various release heights including 2 cm and 3 cm, the three-axis stage was raised to “+66 mm” and “+56 mm” respectively. At each release height,

the average deposition diameter of at least thirty droplets was recorded, and the deposition radius was obtained as a result of dividing the diameter by two. The dynamics of the deposition process and the dimensions were recorded with an EOS C70 camera and a vernier caliper. Deposition details were demonstrated using a scanning electron microscope (ZEISS SIGMA/VP) and the filled rate was measured by ImageJ software. In addition, a compression test was performed by a Universal Testing MTS Machine with the compression velocity of 3 mm/min. A cylinder can only undergo compression once. Therefore, one repetition was performed in the compression experiment. The printed cylinders were based on the same number of droplets and the proposed deposition method. Parameters including load and strain during testing were recorded. Based on the data, the yield strength was obtained.

Chapter 4 Theoretical analysis and results

4.1 Conventional path planning

The basic printing path of Fused Deposition Modeling is the deposition path in a certain direction on the X-Y plane with a Z-axis height. A regular printing path was generated by importing the drawn curved shape into Ultimaker Cura slicing software, as shown in Figure 32.

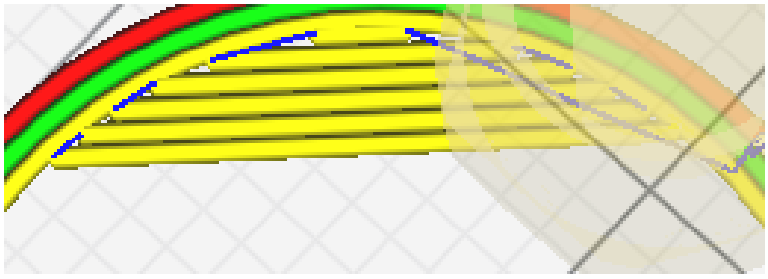

Figure 32. Conventional Printing Path.

The shape in Figure 33 was drawn to illustrate the following equations. As shown in Figure 33, the deposition width of the lines is r_{cg}, and the radius of the cross section (which is a circle) of the object to be printed is R_{cg}.

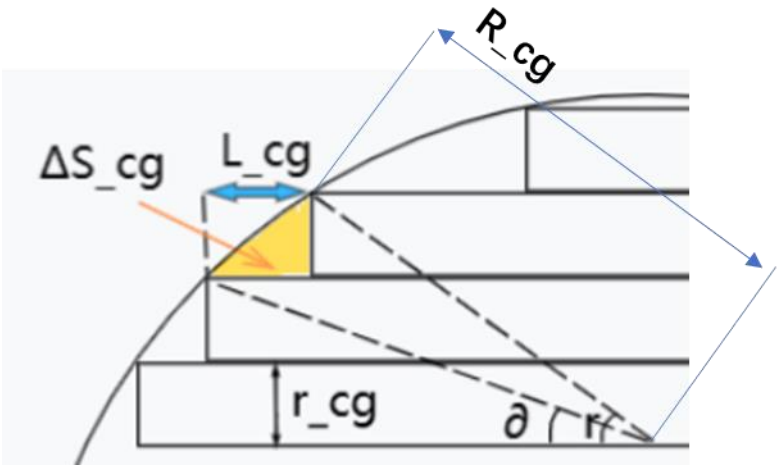

Figure 33. Regular deposition of the circular region.

For the path in the row "n", the unfilled area is in yellow, and the area calculation is based on Figure 33.

$$cos(r_n) = \sqrt{1 - (\frac{R_{cg}|sin\partial_n| + r_{cg}}{R_{cg}})^2} \quad \text{Equation 2}$$

$$L_{cg} = R_{cg}(|cos\partial_n - cos\, r_n|) \quad \text{Equation 3}$$

$$\Delta S_{cg} = \frac{r_{cg}\, R_{cg}(|cos\partial_n| - \sqrt{1-(\frac{R_{cg}|sin\partial_n| + r_{cg}}{R_{cg}})^2})}{2} \quad \text{Equation 4}$$

According to Equation 4, if the radius of the cross section R_{cg} is 100 mm, the red, purple, and black curves represent the deposition widths r_{cg} = 1, 3, 5 mm respectively in Figure 34. Figure 34 was generated in the project based on Equation 4. The result shows that the smaller deposition width will have the smaller unfilled area between the expected and actual deposition. Therefore, the droplet radius in this project should be small. According to Figure 34, the conventional path leads to large dimensional errors, an optimized printing path is proposed for the on-demand printing.

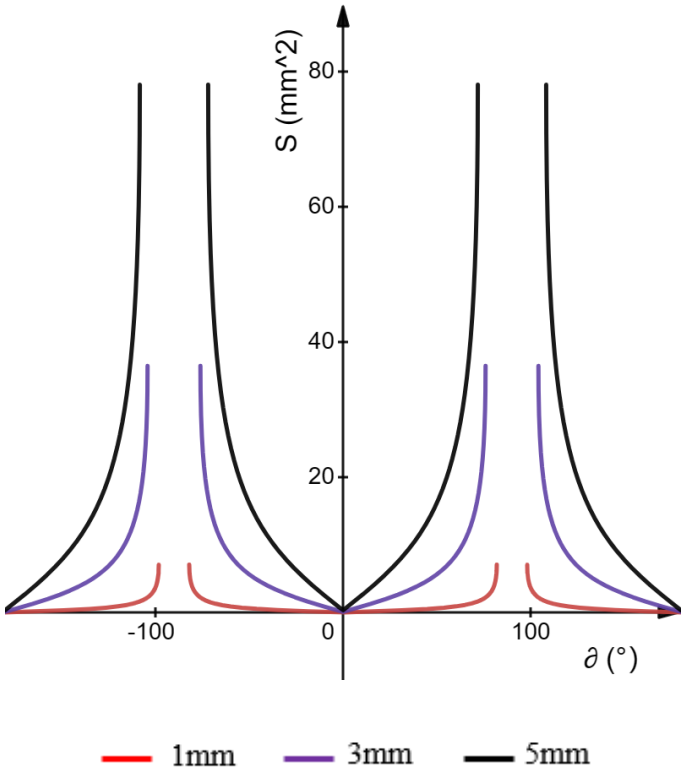

Figure 34. Relationship between the deposition width and the unfilled area.

4.2 Optimized deposition path for curved contours

4.2.1 Non-overlapping-droplet situation

The case of non-overlapping droplets was considered first, and each droplet circle is externally tangent to each other, as shown in Figure 35. The cross-section radius of the object is R, and the droplet deposition radius is w_0 in the top view. The red and blue circles represent the region where the droplets are.

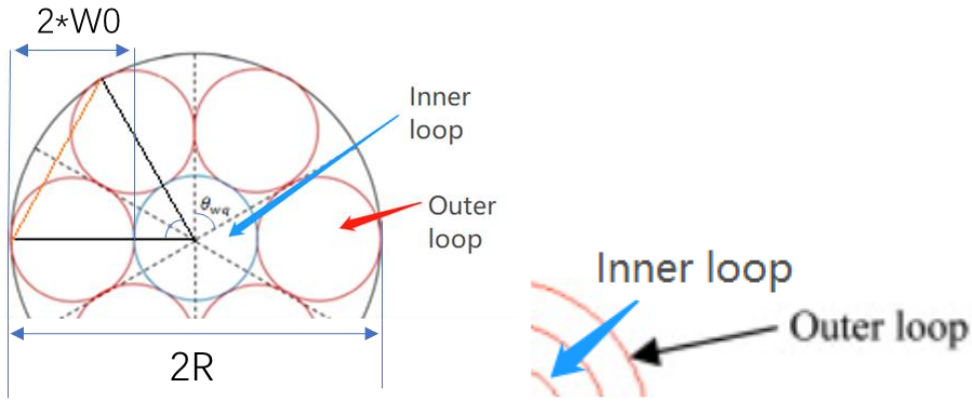

Figure 35. Schematic diagram of droplet landing points.

The angle θ_{wq} corresponding to each red droplet in the outermost loop (the 1st loop) is equal to the angle corresponding to the orange line between two red droplets in Figure 35.

$$\theta_{wq(1)} = 2\ arcsin\frac{w_0}{R-w_0} \qquad \text{Equation 5}$$

The corresponding angle for the second loop from the outermost to the inside is given by,

$$\theta_{wq(2)} = 2\ arcsin\frac{w_0}{R-3w_0} \qquad \text{Equation 6}$$

In the nth loop, the angle is,

$$\theta_{wq(n)} = 2\ arcsin\frac{w_0}{R-(2n-1)w_0} \qquad \text{Equation 7}$$

In the project, the droplets need overlap for combining. Therefore, the angle corresponding to the optimized path $\theta_{r(n)}$ fulfils the following condition,

$$\theta_{r(n)} < \theta_{wq(n)} = 2\ arcsin\frac{w_0}{R-(2n-1)w_0} \qquad \text{Equation 8}$$

4.2.2 Droplet spacing for the line formation

If based on the ideal center-to-center distance w_x calculated in the linear combination of droplets, the top view of two droplets is presented in Figure 36.

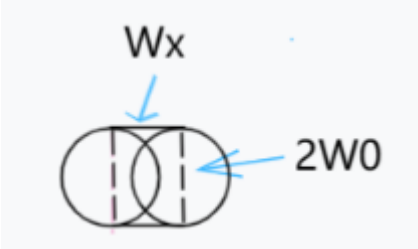

Figure 36. Linear droplet combination.

Based on the linear spacing w_x, the metal-droplet on demand manufacturing encounters problems when the object's cross-section is circular or curved, as shown in Figure 37. The objects formed by subsequent droplets have stacking problems, where the purple area in the middle overlaps excessively leading to an extra surface height variation in the side view, especially for multiple loops inside.

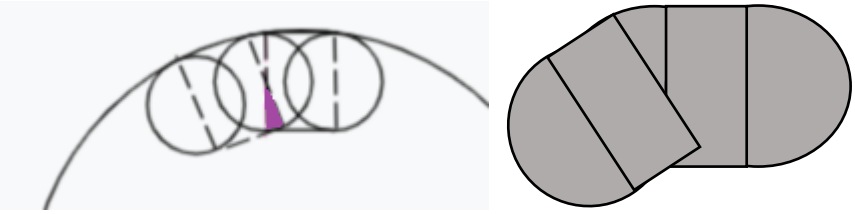

Figure 37. Schematic diagrams of multiple droplets to print curved shapes.

In terms of the constant linear spacing, the angle corresponding to the linear droplet-spacing in the different loops is $\theta_{wx(n)}$. The optimized path with the adaptive spacing $w_{r(n)}$ fulfils the following condition,

$$w_{r(n)} > w_x \quad \& \quad \theta_{r(n)} > \theta_{wx(n)} \qquad \text{Equation 9}$$

4.2.3 Adaptive spacing with angular displacement for curves

A relatively flat layer surface can provide a stable base for the deposition of the upper layers. Based on the above analysis, adaptive spacings for different curvatures are presented as follows.

The cross-sectional radius of the object to be manufactured is R and the droplet radius after deposition is w_0 in the top view. The distance between two droplets is w_r (the distance between two centers r1 to r2). For droplets in the outermost circular loop, the distance between neighboring droplets is w_{r1}.

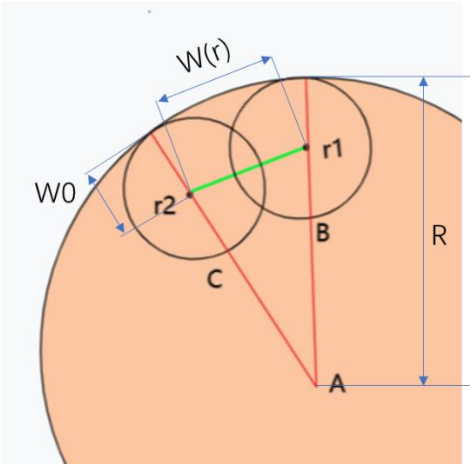

Figure 38. Adaptive spacing for curves.

As shown in Figure 38, the angle $\angle$ CAB between two droplets corresponding to the droplet position in the outermost circular loop is,

$$cos\angle \mathrm{CAB} = cos\,\theta_{r(1)} = \frac{2(R-w_0)^2 - {w_{r1}}^2}{2(R-w_0)^2} \qquad \text{Equation 10}$$

$$\theta_{wx(1)} < \theta_{r(1)} < \theta_{wq(1)} \qquad \text{Equation 11}$$

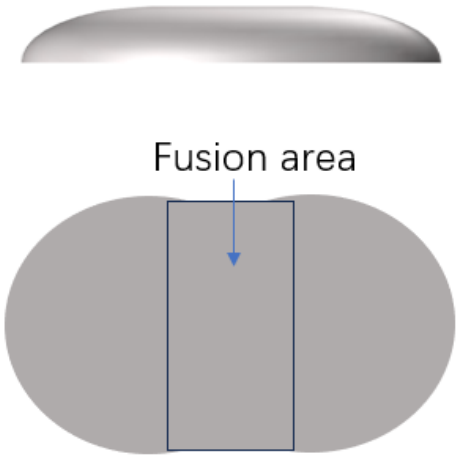

Figure 39. Side and top views of two droplets ideally fusing.

In the case of ideal fusion, the shape in the top view formed by the ideal fusion of the two droplets in the middle approximates a rectangle, as shown in Figure 39.

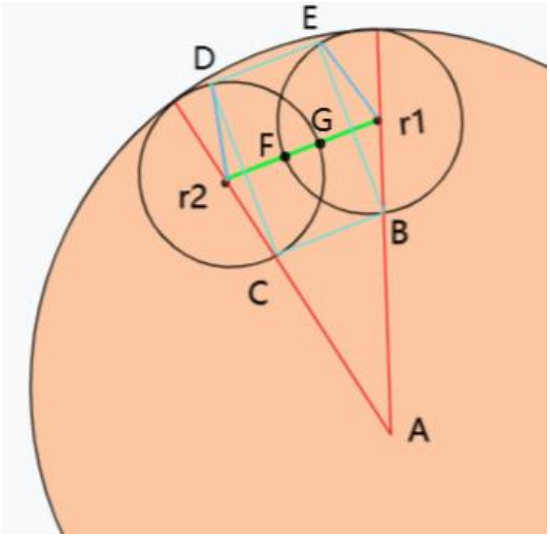

Figure 40. Details of the adaptive spacing for curves.

As shown in Figure 40,

$$\theta_{r(1)} = \angle \mathrm{BAC} \qquad \text{Equation 12}$$

$$BC = w_{r1} - 2w_0 \, sin\frac{\theta_{r(1)}}{2} \qquad \text{Equation 13}$$

Due to the small height of droplets, the fusion area "BCDE" is approximately two sectors minus two triangles,

$$(\pi - \theta_{r(1)})\, {w_0}^2 - 2{w_0}^2\, cos\frac{\theta_{r(1)}}{2}\, sin\frac{\theta_{r(1)}}{2} = 2BC \times w_0\, cos\frac{\theta_{r(1)}}{2} \quad \text{Equation 14}$$

where the sectors are ⌓r_2DGC and ⌓r_1EFB, and the triangles are Δr_2DC, Δr_1BE.

$$2BC \times\ cos\frac{\theta_{r(1)}}{2} = 2\, cos\frac{\theta_{r(1)}}{2} w_{r1} - 4\, w_0 cos\frac{\theta_{r(1)}}{2}\, sin\frac{\theta_{r(1)}}{2} \quad \text{Equation 15}$$

Therefore, the adaptive spacing in the outermost loop is,

$$w_{r1} = \frac{(\pi - \theta_{r(1)} + \sin\theta_{r(1)})\, w_0}{2cos\frac{\theta_{r(1)}}{2}} \quad \text{Equation 16}$$

Three deposition points are required to form a circular arc. Therefore, the angle between neighboring droplet circles ranges from 0 to 120° (0 to 2.09 rad). As shown in Figure 41, when w_0 is 1 mm, the adaptive spacing gradually increases to 1.91 mm as the angular displacement $\theta_{r(1)}$ grows to 2.09 rad.

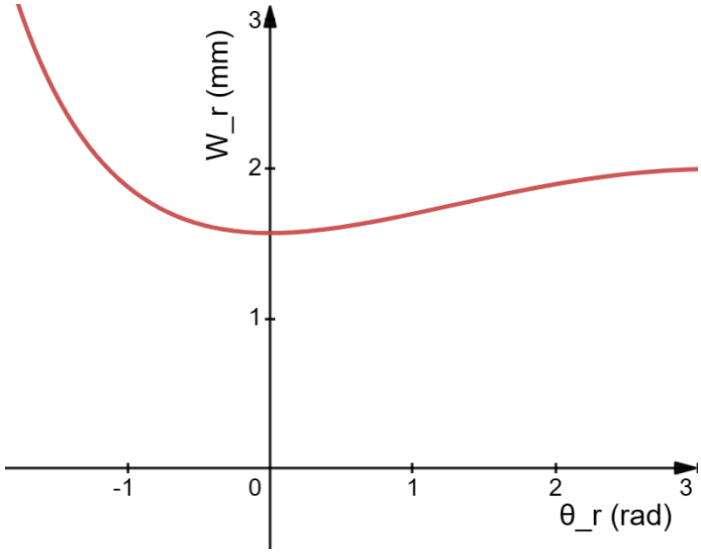

Figure 41. Relationship between w_r and θ_r.

When the deposition platform reaches the end arc, there may be residual angles, for example in a complete circle, $m \times \theta_{r(1)} \leq 360^0$, and $(m+1) \times \theta_{r(1)} > 360^0$ (m is a positive integer). When the angle corresponding to the cross-section arc of the printed object is θ_{rp}, and $\frac{\theta_{rp}}{\theta_{r(1)}} =$ m, no further optimization is required.

If m<$\frac{\theta_{rp}}{\theta_{r(1)}}$<m+1, for the contour closure, the residual angle is equally distributed to each droplet displacement.

$$\begin{cases} {\theta_{r(1)}}' = \frac{\theta_{rp}}{m}, \left|\frac{\theta_{rp}}{\theta_{r(1)}} - m\right| < |-\frac{\theta_{rp}}{\theta_{r(1)}} + m + 1| \\ {\theta_{r(1)}}' = \frac{\theta_{rp}}{m+1}, \left|\frac{\theta_{rp}}{\theta_{r(1)}} - m\right| \geq |-\frac{\theta_{rp}}{\theta_{r(1)}} + m + 1| \end{cases}$$

Equation 17

which means the equal angle variation for the corresponding loop.

Therefore, the method is called “adaptive spacing with angular displacement”, abbreviated as ASAD. When the cross-section center of the printed object in the current layer has the coordinate (x_A, y_A), the center position of the n^{th}droplet in the outermost circular loop is,

$$position_{(n)} = \begin{Bmatrix} x_A & + (R - w_0)\sin\left((n-1)\,{\theta_{r(1)}}'\right), \\ y_A & + (R - w_0)\cos\left((n-1)\,{\theta_{r(1)}}'\right) \end{Bmatrix}$$

Equation 18

If the spacing d_{sc} between each droplet deposition is constant in the inner and outer loops, an example is presented in Figure 42.

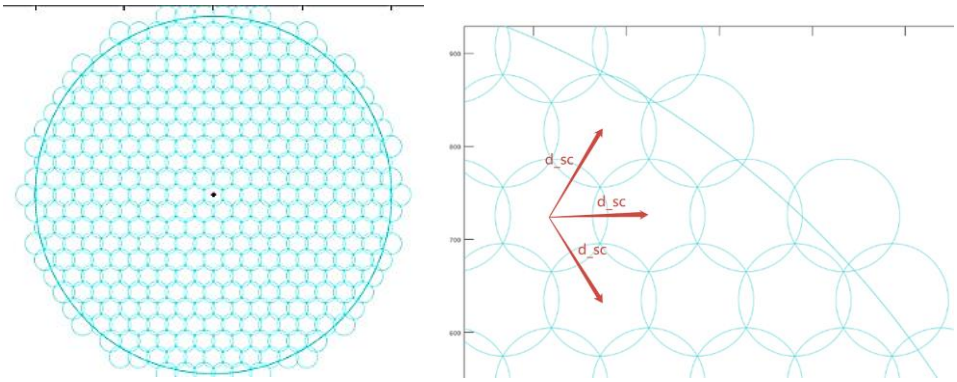

(a) (b)

Figure 42.(a) Constant spacing $d_{sc} = \sqrt{3w_0}$ (b) Local enlarged view.

To cover the entire circular printing area, the accuracy of approximating curved contours is relatively low, as shown in Figure 42, which adds additional roughness in the outer contours. Therefore, the adaptive spacings for the inner circular loops need to be further determined.

When the outermost circular loop is formed based on the adaptive spacing, the side close to the center of the printed object approximates an equilateral polygon in the green area, as shown in Figure 43 (a).

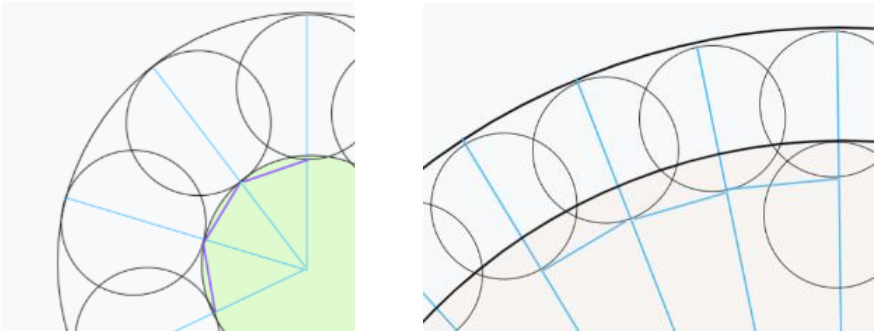

(a) (b)

Figure 43. (a) Inner filling (b) inner droplet bonding.

To avoid voids in adjacent contours, the droplets in the inner loops and surrounding loops need to be combined, as shown in Figure 43 (b). Since the droplet unit is small, two droplets form a short line segment on a circular arc. According to the finite element microelement method, the spacing between two neighboring segments can be determined, as shown in Figure 44.

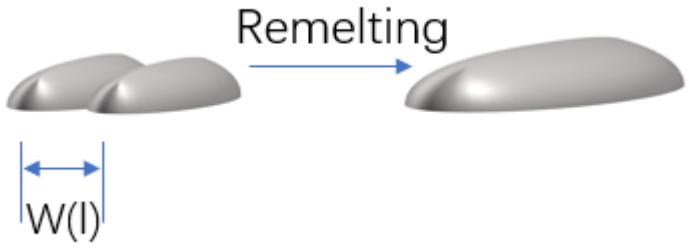

Figure 44. Combination of neighboring segments.

The cross-sectional area in the side view formed by remelting between metal line segments can be represented by the product of the droplet height and the theoretical spacing between metal lines. Therefore, the spacing between metal segments is [52],

$$w_l = \frac{R_i \times (\theta - sin\theta cos\theta) \times \sqrt[3]{\frac{4}{(cos\theta+2)(1-cos\theta)^2}}}{1-cos\theta} \quad \text{Equation 19}$$

where the parameters are shown in Figure 45.

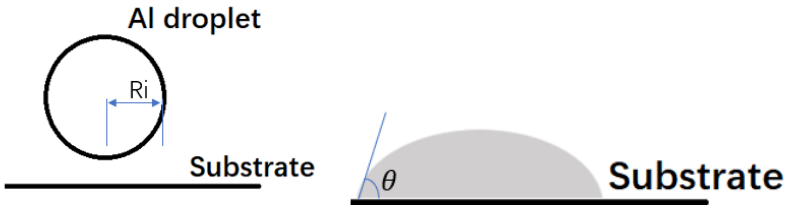

Figure 45. Droplet deposition.

Therefore, the printing area of the second loop from outside to inside is a curved region with a radius of $R - w_l$, which is the orange area in Figure 43 (b).

The angle $\theta_{r(2)}$ between two droplet centers in the second loop is,

$$cos\,\theta_{r(2)} = \frac{2(R-w_0-w_l)^2-{w_{r2}}^2}{2(R-w_0-w_l)^2}, \theta_{wx(2)} < \theta_{r(2)} < \theta_{wq(2)} \quad \text{Equation 20}$$

The center of each droplet in the second loop is determined based on the identical angular displacement. In the n[th] loop, the concentric circle area has a circle radius of $R-(n-1)w_l$. Ultimately, the location of all droplets which are supposed to be deposited can be determined. Depending on the deposition radius and the angular displacement, the corresponding spacing can be determined. Overall, the relationship among the adaptive spacing w_r, the droplet deposition radius w_0 and the angular displacement θ_r is shown in Figure 46, generated in the project using MATLAB R2022b.

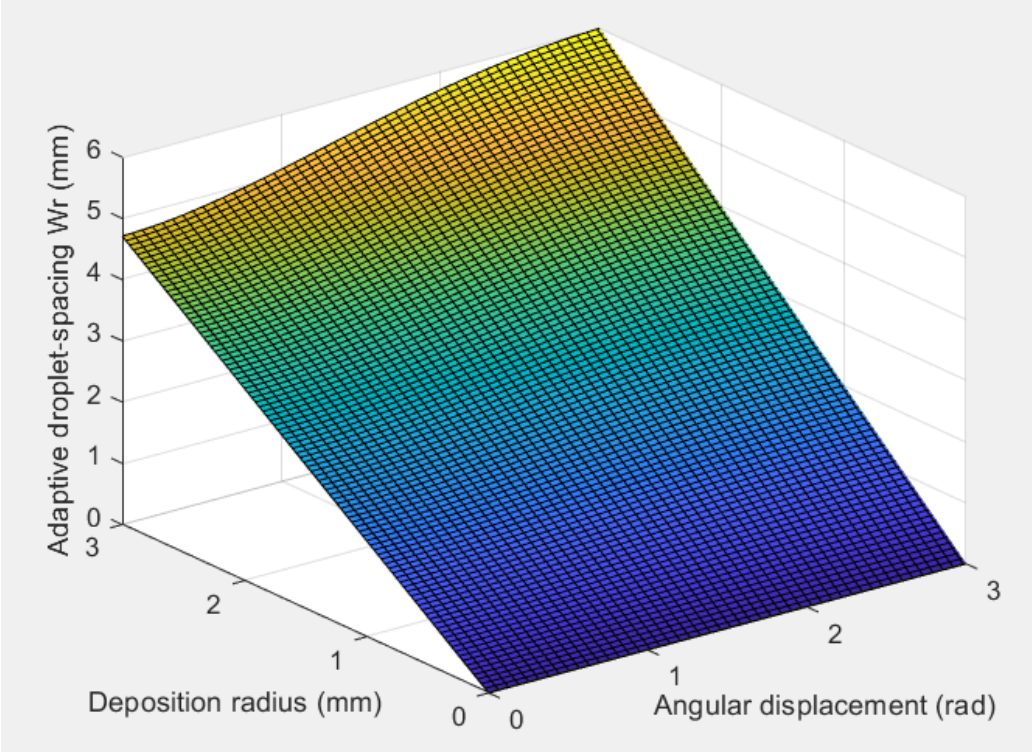

Figure 46. Relationship among w_r, w_0 and θ_r.

In terms of the desired central region for printing, there are three possible situations.

Case 1: $R - n\,w_l \leq w_0$, a single droplet can be deposited, as shown in Figure 47 (a), where the pink area represents the desired central region to be filled.

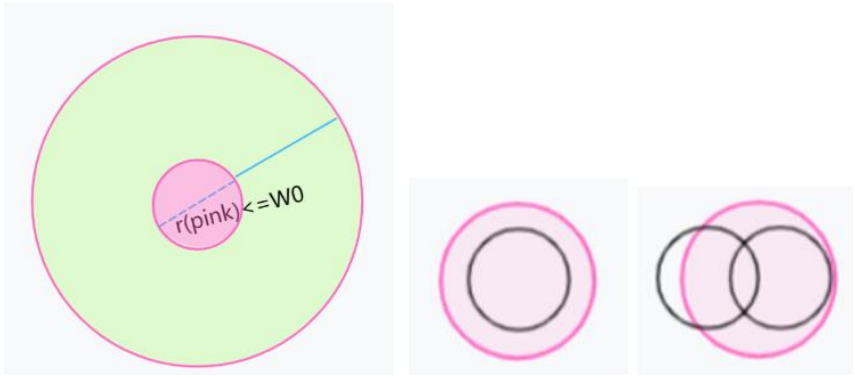

(a) (b) (c)

Figure 47. (a) $r(pink) \leq w_0$; (b) & (c) $r(pink) = \sqrt{2}w_0$.

Optimization for case 1: When $R - n\,w_l$ is less than w_0, smaller sized droplets can be deposited to avoid excessive overlap.

Case 2: $w_0 < R - n\,w_l < w_0 + \frac{w_r}{2}$, an instance of the case 2 is presented in Figure 47 (b) & (c), where the black circles represent droplets in the top view. If the metal printing material is required to be saved, the second metal droplet cannot be deposited even if the radius of the center region is $\sqrt{2}w_0$. Since $w_0 < w_r$(that is $\frac{w_0}{2} < \frac{w_r}{2}$), $w_0 + \frac{w_r}{2} > 1.5w_0 > \sqrt{2}w_0$. In Figure 47 (b), the filled rate for the pink central region is only 50%.

To increase the filled area, a second metal droplet can be deposited. As shown in Figure 48, $r(pink) = w_0 + p$ ($p < \frac{w_r}{2}$), and the area of the pink area S_p is $\pi(p + w_0)^2$.

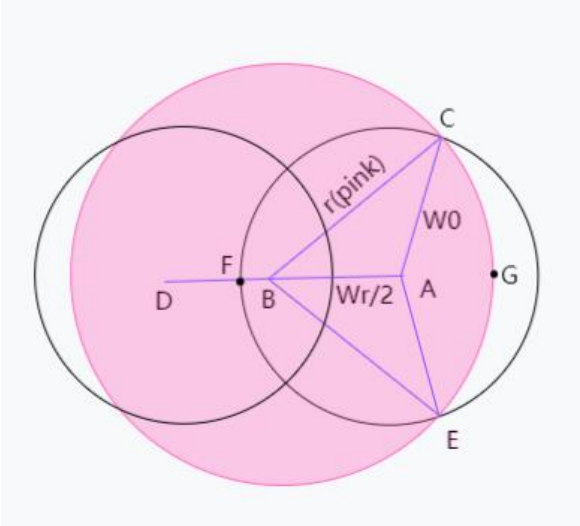

Figure 48. $r(pink) = w_0 + p$.

For $\backsim BCGE$, $BA = \frac{w_r}{2}$.

$$cos\ \angle CBA = \frac{r(pink)^2 + (\frac{w_r}{2})^2 - {w_0}^2}{r(pink) \times w_r} \quad \text{Equation 21}$$

$$S_{\backsim BCGE} = \arccos\ (cos \angle CBA) \times\ r(pink)^2 \quad \text{Equation 22}$$

For $\backsim ACFE$, $AF = AC = w_0$.

$$cos\ \angle BAC = \frac{{w_0}^2 + (\frac{w_r}{2})^2 - r(pink)^2}{w_0 \times w_r} \quad \text{Equation 23}$$

$$S_{\backsim ACFE} = \arccos\ (cos \angle BAC) \times\ {w_0}^2 \quad \text{Equation 24}$$

For ΔBAC,

$$p_{BAC} = \frac{2(r(pink) + w_0) + w_r}{4} \quad \text{Equation 25}$$

$$S_{BAC} = \sqrt{p_{BAC}(p_{BAC} - r(pink))(p_{BAC} - w_0)(p_{BAC} - \frac{w_r}{2})} \quad \text{Equation 26}$$

If the requirement is to obtain the possible full coverage, the deviation in the center region can be distributed equally to w_l in order to create a new ${w_l}'$, where $w_l' = w_l + \frac{r(pink) - w_0}{n}$.

Case 3: $R - n\,w_l \geq w_0 + \frac{w_r}{2}$, or if $w_l \gg \left(w_0 + \frac{w_r}{2}\right)$. When $R - (n-1)w_l = r(pink) = w_0 + \frac{w_r}{2}$, two droplets can be deposited as shown in Figure 49.

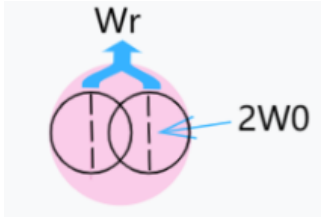

Figure 49. $r(pink) = w_0 + \frac{w_r}{2}$.

The area of the center region S_p is $\pi\left(w_0 + \frac{w_r}{2}\right)^2$ in Figure 49, and the area of two droplets combined S_{2d}. Hence, the proportion of the filled area in the center region is $\frac{S_{2d}}{S_p}$.

4.3 Analysis of droplet deposition

The energy conversion of aluminum droplets is different from that in water droplets with low surface tension, and hence an energy model for aluminum droplet deposition with high surface tension was developed for the purpose of studying the relationship between the release height and the deposition radius etc. In the study, the properties of aluminum droplets are presented in Table 5.

Table 5. Properties of aluminum droplets at 900 ℃.

Properties	Values
Density ρ_i $\left(\frac{kg}{m^3}\right)$ [74]	2302
Viscosity η (mPa · s) [74]	0.894
Heat Capacity C_l $\left(\frac{J}{kg \cdot K}\right)$ [75]	1086
Thermal Conductivity k_l $\left(\frac{W}{m \cdot K}\right)$ [75]	96.4
Surface tension σ_{lg} $\left(\frac{N}{m}\right)$ [76]	0.88

1) Initial stage

The total initial energy E_{ini} of an aluminum droplet consists of the initial kinetic energy E_k, the gravitational potential energy E_p and the surface energy E_s.

$$E_{ini} = E_k + E_p + E_s \qquad \text{Equation 27}$$

$$E_k = \frac{1}{2} m v_0^2 = \frac{1}{2} \rho_i V_i v_0^2 \qquad \text{Equation 28}$$

where m is the mass of one droplet, V_i is the volume of the droplet and v_0 is the initial velocity of the droplet, approximated as the descending speed of the wire feeder v_{sd}.

$$E_p = mgH = \rho_i V_i g H \qquad \text{Equation 29}$$

where H is the release height.

As shown in Figure 50 (a), the sphere radius before impact is R_i (0.8 mm in the project), and hence the surface energy before impact is,

$$E_s = 4\sigma_{lg}\pi R_i^2 \qquad \text{Equation 30}$$

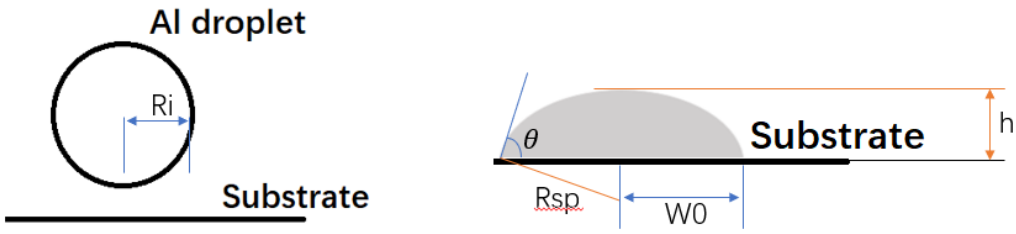

(a) (b)

Figure 50. (a) Droplet falling (b) deposition.

The droplet mass produced by a travel of the wire feeder is conserved.

$$\rho_i V_i = \frac{4}{3}\pi\rho_i {R_i}^3 = \rho_{ng}\frac{\pi(d_{sd}-d_{su}){d_{wire}}^2}{4} \qquad \text{Equation 31}$$

where ρ_{ng} is the density of the aluminum wires [77].

The shape of a free-falling droplet is approximated as a sphere, and the Nusselt number of free-falling droplets is approximated as [78],

$$Nu = 2 + 0.6\sqrt{Re}\,\sqrt[3]{Pr} \qquad \text{Equation 32}$$

where $Re = \frac{2\rho_i v_{dn} R_i}{\eta}$; $Pr = \frac{C_l \eta}{k_l}$; v_{dn} is the droplet velocity.

The reason for the Nusselt number greater than 2 is the contribution of flow over the sphere on heat transfer, based on past experimental statistics on the spherical shape [78].

Since $Nu = \frac{2h_l R_i}{k_{\acute{a}j}}$, where h_l is convective heat transfer coefficient in the boundary layer of aluminum droplets, and $k_{\acute{a}j}$ is environmental thermal conductivity $0.0267\left(\frac{W}{m\cdot K}\right)$, the corresponding Biot number is,

$$Bi = \frac{2h_l R_i}{k_l} \qquad \text{Equation 33}$$

For the release heights from 0.01 to 0.03 m, the Biot number results are 0.0023 to 0.0026, which is much less than 0.1. Therefore, it could be assumed that the temperature of the falling droplets is uniform. The falling process could be simplified to be affected by the parameter h_l, and the solidification time estimated in the falling process is,

$$t_{li} = \frac{mC_l}{h_l A} \qquad \text{Equation 34}$$

where A is the surface area of an aluminum droplet.

If the droplets continue to fall in the environment, the solidification time will be 4.16 to 4.76 seconds based on the release heights from 0.01 to 0.03 m. This is much higher than the experimental falling time, which was roughly 0.01 to 0.04 seconds for the release heights from 0.01 to 0.03 m, and hence the aluminum droplets were approximately deposited on the substrate in liquid phase.

2) Impact of droplets on the substrate

As shown in Figure 50 (b), the curved surface area of the spherical cap is,

$$S_{cap} = 2\pi R_{sp} h \qquad \text{Equation 35}$$

$$R_{sp} = \frac{h}{1-cos\theta} = \frac{w_0}{sin\theta} \qquad \text{Equation 36}$$

The bottom area of the droplet is,

$$S_{bottom} = \pi {w_0}^2 \qquad \text{Equation 37}$$

The converted surface energy can be expressed as,

$$E_s' = 2\sigma_{lg}\pi R_{sp} h + (\sigma_{ls} - \sigma_{sg})\pi {w_0}^2 \qquad \text{Equation 38}$$

According to Young's Equation,

$$\sigma_{lg} cos\theta = \sigma_{sg} - \sigma_{ls} \qquad \text{Equation 39}$$

Therefore, the calculated surface energy is,

$$E_s' = \pi\sigma_{lg}(2R_{sp} h - cos\theta {w_0}^2) \qquad \text{Equation 40}$$

In the deposition, viscous dissipation is,

$$W_V' = \int_0^{t_n} \int_V \phi \, dV_n \, dt \approx \phi \, V_n t_n \qquad \text{Equation 41}$$

where ϕ is the average viscous dissipation function, V_n is the volume of viscous fluid and t_n is the viscous dissipation time.

$$\phi = \eta \left(\frac{\partial v_i}{\partial x_j} + \frac{\partial v_j}{\partial x_i} \right) \frac{\partial v_i}{\partial x_j} \approx \eta \left(\frac{v_{dn}}{\delta} \right)^2 \qquad \text{Equation 42}$$

where η is the viscosity, δ is the boundary layer thickness, and $\frac{dv}{dy}$ is the boundary layer normal velocity gradient. Chandra and Avedisian [79] predicted a maximum spreading diameter of droplets, however with an error of 40%. Therefore, their assumed thickness was not accurate.

For the velocity at the instant of the droplet deposition,

$$\rho_i V_i g (H - R_i) = \frac{1}{2} \rho_i V_i (v_{dn}^2 - v_0^2) \qquad \text{Equation 43}$$

$$v_{dn} = \sqrt{2g(H - R_i) + v_0^2} \qquad \text{Equation 44}$$

Pasandideh-Fard et al. [80] calculated the dimension of the boundary layer to be,

$$\delta = \frac{4R_i}{\sqrt{Re}} \qquad \text{Equation 45}$$

where Re is Reynolds number, and $V_n = \pi {w_0}^2 \delta$.

In the mathematical model of Pasandideh-Fard et al., they measured the time at maximum droplet spreading t_m, by observing the trajectory of the droplets in their experiments. The solidification time t_n is greater than t_m, and there is the

dissipation prior to the solidification, and hence the dissipation time is near the solidification time.

The solidification time is [81],

$$t_n \approx \frac{C_l \rho_i {R_i}^2}{k_l} \left(\frac{L_l}{C_l(T_m - T_s)} + \frac{T_i - T_m}{T_m - T_s}\right) \quad \text{Equation 46}$$

where L_l is the latent heat, and T_m, T_s, T_i are the melting point of aluminum droplets, the substrate temperature, and the heated droplet temperature respectively.

In the energy model of the project, the change in gravitational potential energy was modified to be the displacement between the droplet centroids for the release and deposition positions. The mass center of the homogeneous spherical cap is on the central axis and the centroid height is,

$$h_C = \frac{h(2{w_0}^2 + h^2)}{6{w_0}^2 + 2h^2} \quad \text{Equation 47}$$

The gravitational potential energy for the deposition is,

$$E_p' = \rho_i V_i g h_C \quad \text{Equation 48}$$

Therefore, the converted energy E_{ce} is,

$$E_{ce} = E_s' + W_V' + E_p' \quad \text{Equation 49}$$

Preliminary tests were carried out to observe the deposition of droplets at different heights. As shown in Figure 51, oscillation existed during the deposition process of droplets.

Figure 51. Droplet deposition in the experiments.

At low release heights, the deposition shape eventually formed a spherical cap, as shown in Figure 52.

Figure 52. Final deposition in experiments.

However, when the release height was greater than 0.1 m, the droplets solidified before the end of the oscillation due to the strong impact, as shown in Figure 53. Therefore, the final release height was selected within 0.03 m.

Figure 53. SEM image of a solidified droplet before the end of the oscillation.

As shown in Figure 54, the deposition radius obtained in the project is positively correlated with the release height. The dashed line is a trend line, and therefore, the deposition radii at other release heights can be also approximately estimated.

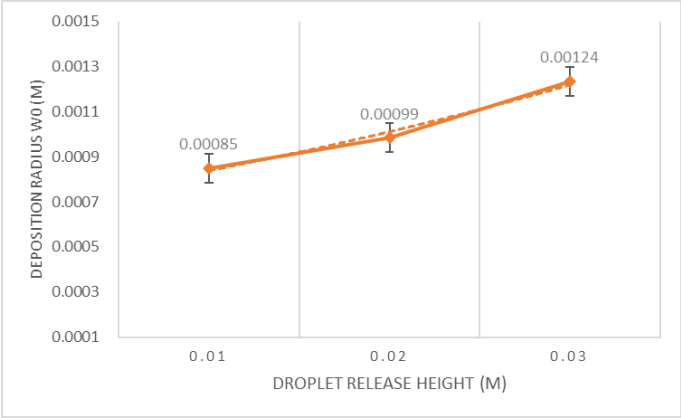

Figure 54. Relationship between the droplet release height and the deposition radius.

Based on the values presented in Table 3 & 4 & 5, with the obtained deposition diameters, the corresponding values in Table 6 were derived.

Table 6. Droplet energy values in experiments.

Release height (m)	E_p **(J)**	E_s **(J)**	E_k **(J)**	E'_p **(J)**	E'_s **(J)**	W'_V **(J)**	**Relative difference**
0.01	5.03E-07	7.26E-06	5.68E-07	2.44E-08	6.73E-06	8.11E-07	9.07%
0.02	1.01E-06	7.26E-06	5.68E-07	2.07E-08	6.20E-06	1.83E-06	8.81%
0.03	1.51E-06	7.26E-06	5.68E-07	1.40E-08	4.12E-06	4.01E-06	12.67%

As shown in Table 6, the unit for energy is the joule (J), and the relative difference is between the initial E_{ini} and the converted energies E_{ce}, which is $\frac{E_{ini}-E_{ce}}{E_{ini}}$ in percentage.

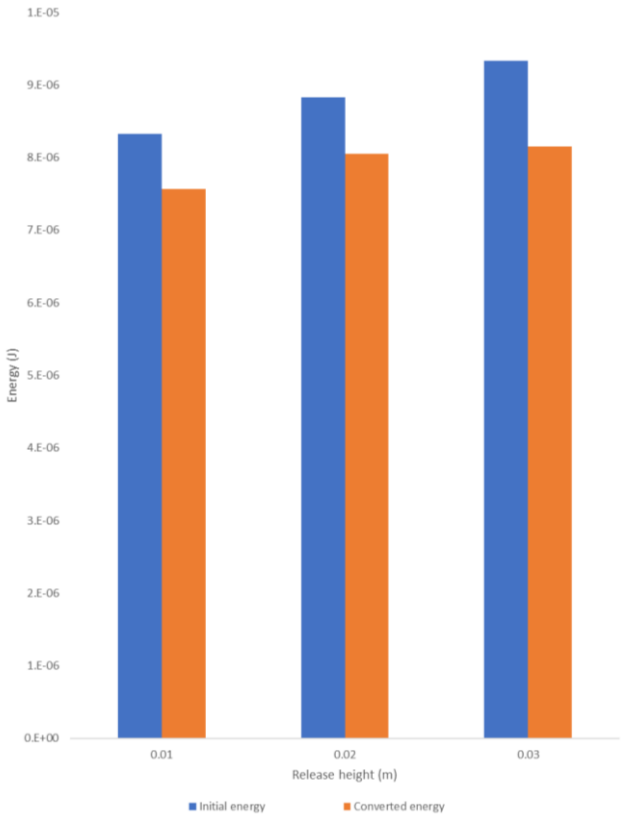

Figure 55. Initial and converted droplet energy at different release heights.

Figure 55 shows the initial and converted droplet energy at different release heights, based on the data in Table 6. As shown in Figure 55, the work to overcome air resistance resulted in a loss of the mechanical energy, and hence the converted droplet energy was slightly less than the initial energy. The greater displacement through the air led to more energy loss in the droplets. When the release height is low, $E_{ini} \approx E_{ce}$, and a relationship can be obtained based on the droplet release height, the initial droplet size and the deposition radius,

$$\rho_i V_i g h_C + \pi\sigma_{lg}\left(2\frac{h^2}{1-cos\theta} - cos\theta {w_0}^2 - 4R_i^2\right) + \frac{\eta\, t_n\, \pi {w_0}^2 {v_{dn}}^2\sqrt{Re}}{4R_i} - \frac{1}{2}\rho_i V_i v_0^2 \approx \rho_i V_i g H$$

Equation 50

The droplet deposition process is a transformation among surface energy, kinetic energy, gravitational potential energy and viscous dissipative energy. The proposed model can present the energy conversion of the deposition. Under the condition that the same sized droplets were released at different heights, the energy proportion changes are shown in Figure 56. The values presented in Figure 56 are based on the data in Table 6.

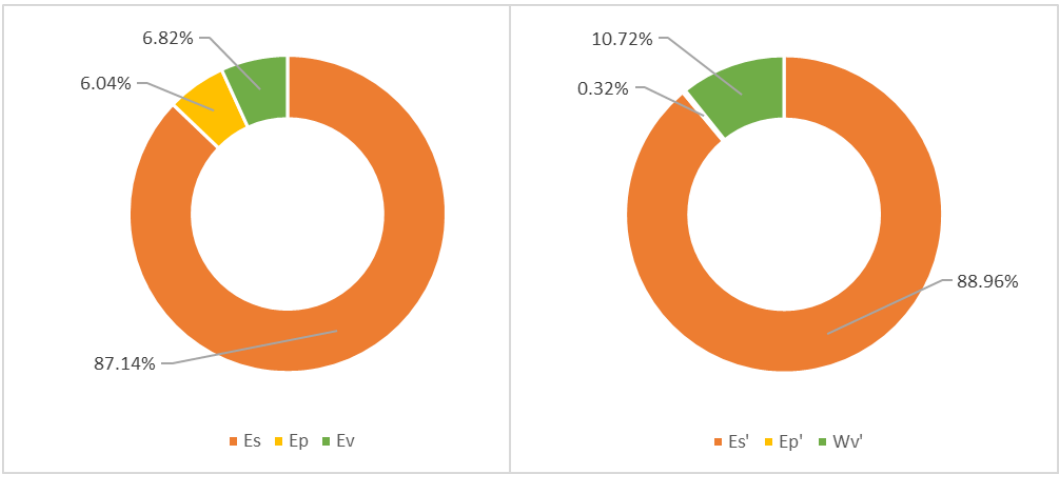

(a) 0.01 m

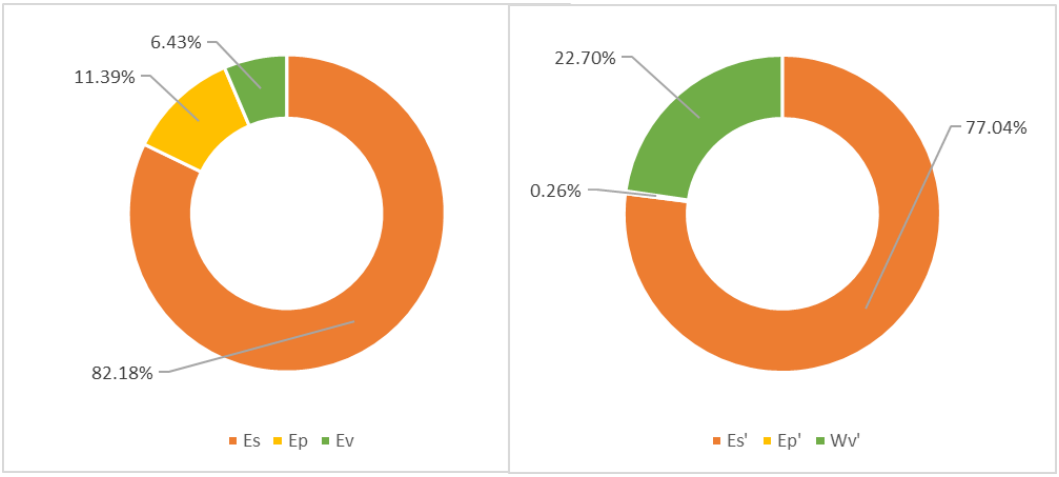

(b) 0.02 m

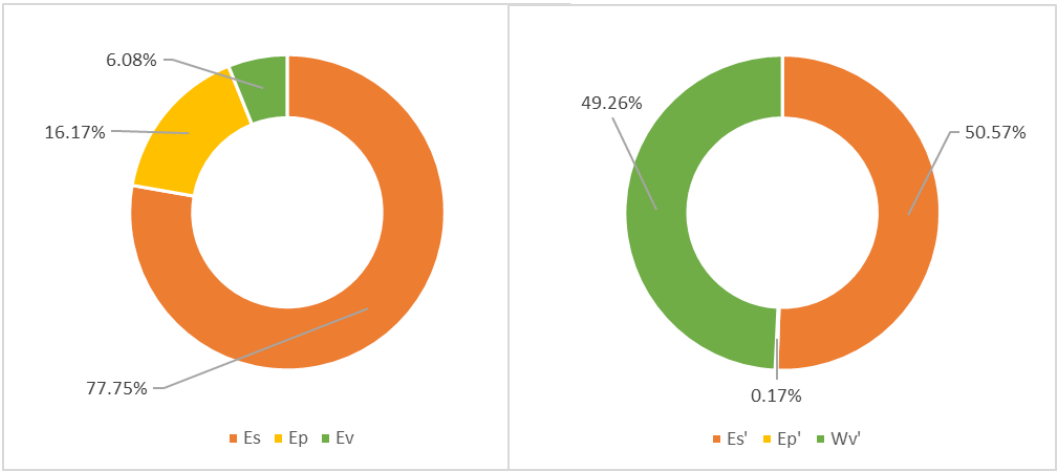

(c) 0.03m

Figure 56. Percentage of energy in the initial and converted energies at (a) 0.01, (b) 0.02, (c) 0.03m.

The surface energy ratio varied greatly due to the shape change, and the release height was one of the significant factors in determining the droplet deposition radius. The proportion of the viscous dissipation increased significantly as the release height ascended.

Dynamic changes in the droplet energy are presented, providing a tool for the analysis of the deposition behavior. In addition, the droplet deposition radius at different heights was obtained, which determined the practical spacing of neighboring droplets in the path planning.

4.4 Single droplet deposition and multi-droplet linear combination

When the droplet size was large, the volume of gas drawn into the bottom of the droplet was great, resulting in a significant phenomenon of gas pores, as shown in Figure 57.

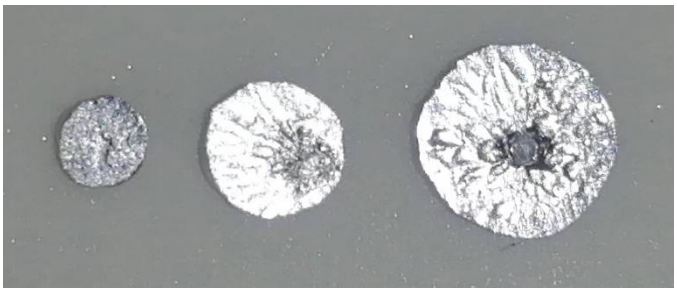

Figure 57. Gas pores in droplets.

According to the droplet analysis by Liu et al. [82], random collapses occurred locally at the bottom on account of the Kelvin Helmholtz instability. As a result, the two larger droplets, in the center and on the right of Figure 57, were found to have a random number of hollows, and the hollow locations were dispersed.

The gas pores reduced the surface quality of the parts. For this reason, small droplets were required. For instance, the smallest droplets that could be stably printed had a radius of 0.99 to 1 mm on the deposition plate at the droplet release height of 0.02 m based on the system in the project.

As shown in Figure 58, shallow depressions were on the bottom surface of the smallest droplet with no obvious formation of gas pores.

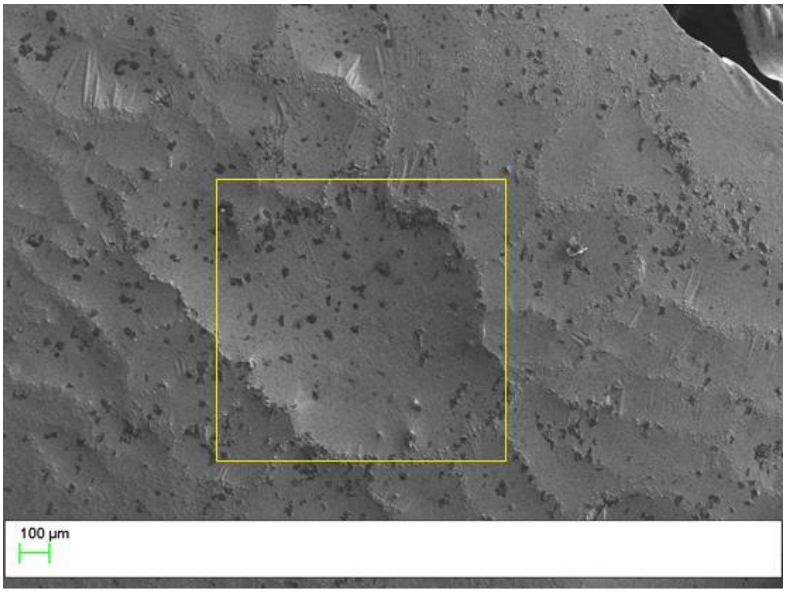

Figure 58. SEM image of the bottom surface.

Irregular shapes were produced occasionally, such as satellite droplets or droplets with tails. As shown in Figure 59, the droplets with tails were created since the retraction speed of the wire feeder was slow, without generating a sufficient instantaneous vacuum.

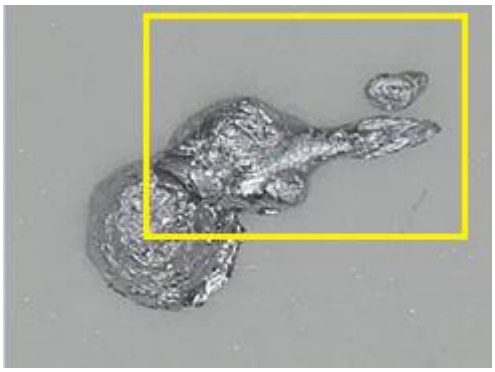

Figure 59. A droplet with tails.

Under room temperature conditions, two droplets could not combine tightly, as shown in Figure 60 (a). Although the neighboring droplets were shaped to fit together, the fitted parts left a narrow gap at the junction, as shown in Figure 60 (b). In addition, Hao et al. found there was a pinhole problem between the droplets and the substrate with a low substrate temperature of roughly 30°C [83]. Based on

simulations [84], the linear deposition of molten droplets was investigated, but the droplets landed on an unheated substrate. As a result, there were gaps in the bonding area between the droplets.

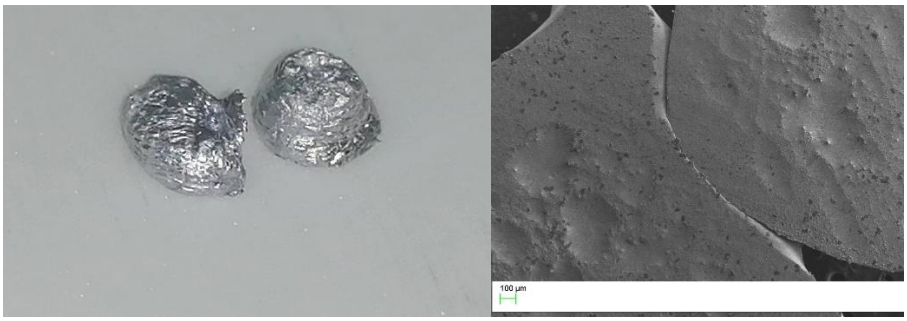

(a) (b)

Figure 60. (a) Two droplets in top view (b) Bottom surface of two droplets in the SEM image.

When the substrate in the project was heated to roughly 400 degrees, there was no obvious gap between droplets, and remelting can be seen in Figure 61. The dashed lines represent the boundaries between the droplets.

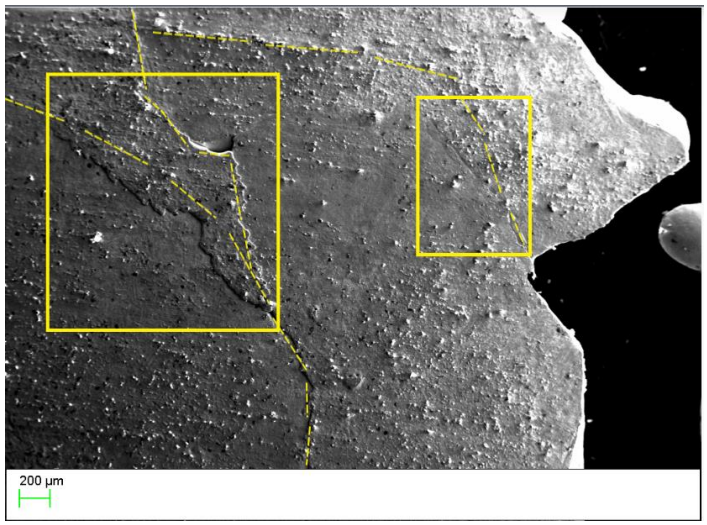

Figure 61. Binding of multiple droplets.

As shown in Figure 62, the release height includes the thickness of the crucible bottom, plus the distance from the crucible bottom to the substrate. The thickness of the crucible bottom is nearly 6 mm. Therefore, the crucible bottom surface and the substrate were approximately close to each other at the release height of 0.01 m. The substrate was affected by the heating itself and the heat

transfer of the heater for melting the aluminum droplets above, which may cause uneven heating for the substrate. During the straight-line printing, the substrate was prone to breakage, as shown in Figure 63.

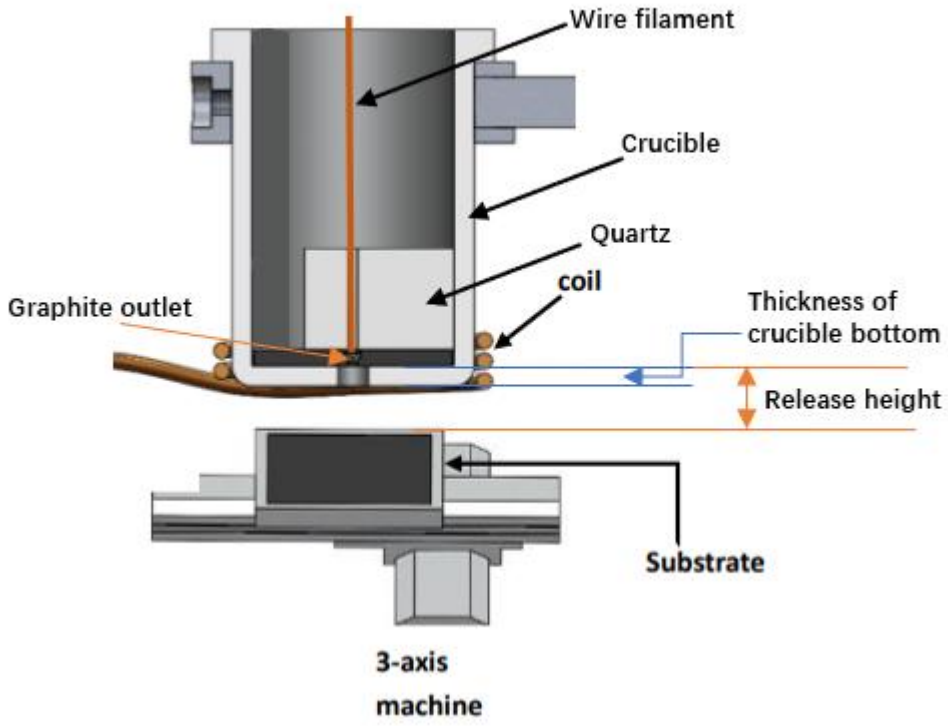

Figure 62. Schematic of the distance between the crucible bottom and the substrate.

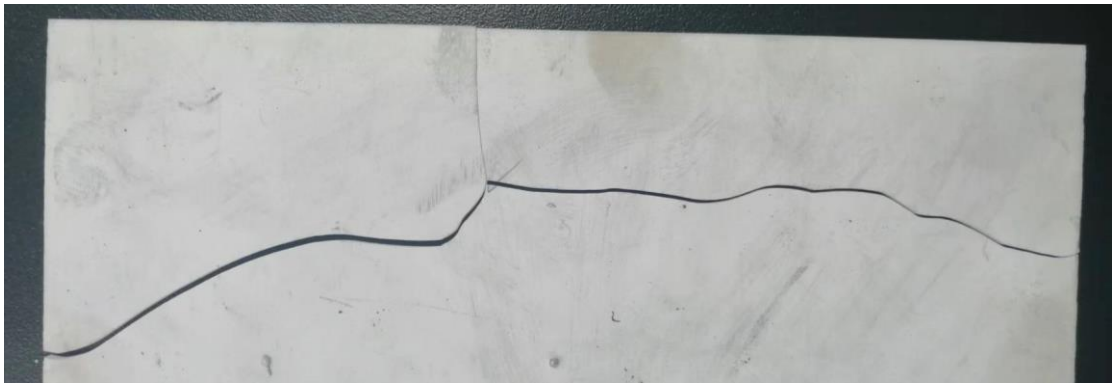

Figure 63. Substrate breakage at low release height.

Therefore, 0.02 m was selected as the release height for the printing. In the straight-line printing, a deflection was observed, as shown in Figure 64. The

deflection in the linear deposition was similar to the morphology in Figure 16. The reason could be that the graphite opening was passively enlarged in Figure 65 by the molten droplets or the aluminum wires, which further led to the deflection. The volume of the graphite outlet would be enlarged with degradation, resulting in the droplet size being affected.

Figure 64. Deflection in the printing.

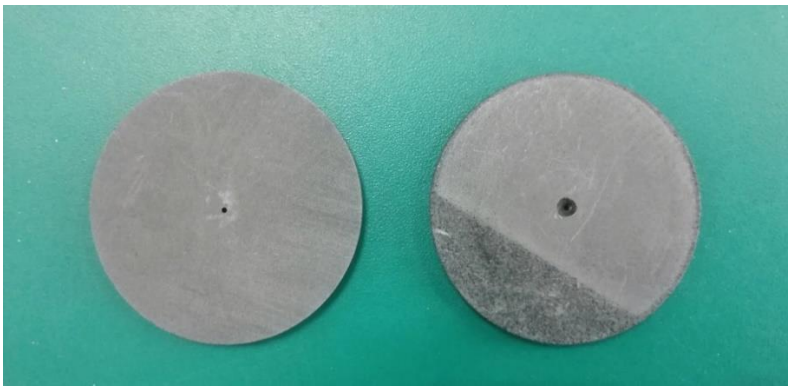

Figure 65. Intact graphite and used graphite.

Primary defects in the manufacture of graphite may cause the surface of the graphite outlet to be uneven or inconsistent in quality. The droplets from the outlet were subjected to the cooling effect of the environment, which could lead to solidification and blockage in the outlet channel. In addition, small amounts of

solidified aluminum remained at the outlet of used graphite, which further caused different wetting conditions around the outlet, as shown in Figure 66 (a).

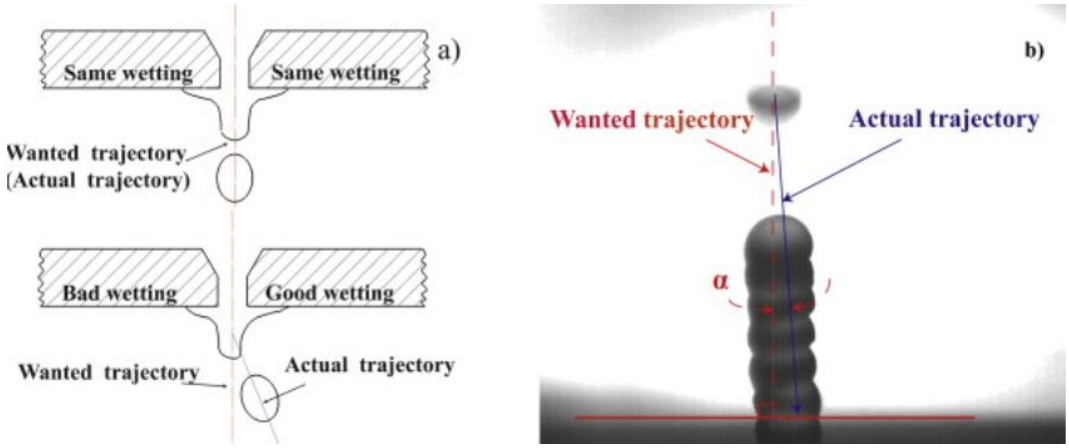

(a) (b)

Figure 66. (a) Schematic diagram (b) droplet flight trajectory [25].

Consequently, the actual trajectory was not entirely consistent with the desired trajectory due to the varying wetting of liquid aluminum at the graphite outlet, as shown in Figure 66 (b).

4.5 Printing of curved shapes

As shown in Figure 67, to print the same circular pattern, the filled rate with the zigzag path is lower than that with the proposed ASAD method since $w_{r(n)} > w_x$. In addition, the printing based on the proposed ASAD method is closer to the curvature of the shape.

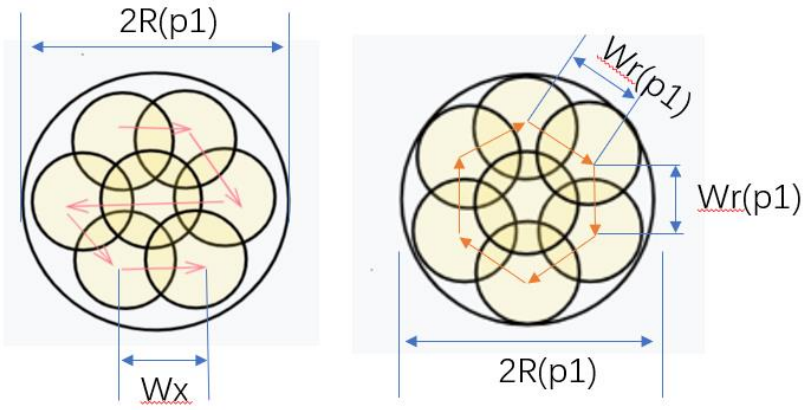

Figure 67. (a) Zigzag path example (b) proposed ASAD method.

For the system with the deflection in the project, according to the zigzag points in Figure 68 (a), the zigzag result is shown in Figure 68 (b). The result indicates the zigzag path approximates the curved contours at low quality.

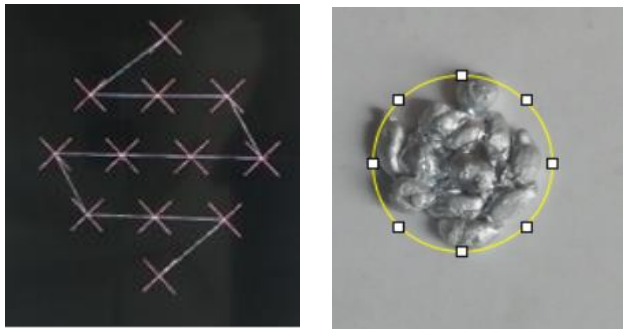

(a) (b)

Figure 68. (a) Deposition points based on the zigzag method (b) zigzag result.

Based on the proposed ASAD method, the theoretical filled rate "FR" for complete filling in the central zone is,

$$FR = 1 - f(voidage) \qquad \text{Equation 51}$$

where $f(voidage)$ is the vacancies in a layer that is not filled. For instance, the area "FGED" is void, as shown in Figure 69.

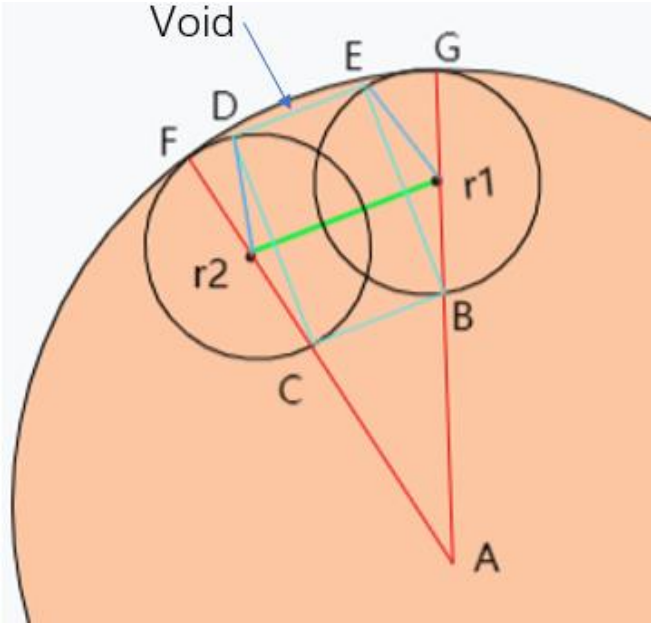

Figure 69. Voids in the printing.

Due to the area S(FGED) = S⌓AFG- S⌓r_1EG -S⌓r_2DF- SΔABC-SΔr_1EB-SΔr_2DC-S(CBED),

$$f(voidage) = \frac{m\left[\frac{\theta_{r(1)}R^2}{2} - (\theta_{r(1)} + sin\theta_{r(1)}){w_0}^2 - \frac{(R-2w_0)^2\, sin\theta_{r(1)}}{2} - (2w_{r1}w_0\, cos\frac{\theta_{r(1)}}{2} - 2{w_0}^2 sin\theta_{r(1)})\right]}{\pi R^2}$$

Equation 52

where “m” is the droplet number in Table 7.

Therefore, the rate is,

$$FR = 1 - \frac{m\left[\frac{\theta_{r(1)}R^2}{2} - \pi{w_0}^2 - (\frac{R^2}{2} + {w_0}^2 - 2Rw_0)sin\theta_{r(1)}\right]}{\pi R^2}$$

Equation 53

which indicates the accuracy of approximating curved shapes.

For a deposition radius of 0.99 mm, the theoretical radius of printed curved patterns and the corresponding angular displacement of droplets in the outermost circular loop are shown in Table 7. Angular displacement can approach infinitesimal, and Table 7 lists a portion. Overlap ratio ($\frac{2w_0-w_r}{w_0}$) is the ratio of the droplet overlapping length to the deposition radius, and theoretical filled rate is proportion of the filled area to the cross-sectional area of the printed object.

Table 7. Theoretical parameters for printed patterns.

Droplet number "m"	**Angular displacement (°)**	**Radius of printed patterns (mm)**	**Overlap ratio**	**Theoretical filled rate**
3	120.0	2.10	9.0%	49.2%
4	90.0	2.27	20.0%	53.7%
5	72.0	2.49	25.0%	59.2%
6	60.0	2.71	29.2%	64.9%
7	51.4	2.93	32.2%	69.9%
8	45.0	3.17	34.3%	74.1%
9	40.0	3.40	36.0%	77.6%
10	36.0	3.64	37.0%	80.4%
11	32.7	3.88	38.0%	82.8%
12	30.0	4.12	38.7%	84.8%
13	27.7	4.36	39.3%	86.5%
14	25.7	4.60	40.0%	88.0%
15	24.0	4.85	40.1%	89.1%
16	22.5	5.09	40.4%	90.1%
17	21.2	5.34	40.6%	91.0%
18	20.0	5.58	40.9%	91.8%
19	18.9	5.83	41.1%	92.5%
20	18.0	6.08	41.2%	93.1%

The greater the curvature, the smaller the corresponding radius of the curved path, and hence the spacing between droplets is increased accordingly to reduce overlap. When the spacing between two neighboring droplets is greater than the droplet deposition diameter, there is no physical connection among neighboring droplets. As a result, a broken line is shown in Figure 13 (a). For the case of three droplets forming a closed contour, the calculated spacing is $1.91w_0$ when the deposition radius is w_0, according to Equation 16. By definition, the curvature of a

straight line is $\frac{1}{\infty}$, approaching zero. In terms of curved shapes with internal filling, the spacing w_r is greater than the spacing in the linear deposition, according to Equation 9. The spacing on curved trajectories is as low as 1.57 w_0, which is the value when the angular displacement approaches zero, using Figure 41 and Figure 46 as references. Therefore, based on the proposed model, the spacing for the curved deposition are from 1.57w_0 to 1.91w_0.

If the radius of curved pattern is between two theoretical radii, the angular displacement can be selected with the corresponding number of droplets by rounding up or down, depending on the requirement.

For the contour-parallel paths with the constant droplet spacing w_x (1.49 mm), the overlap ratio ($\frac{2w_0 - w_x}{w_0}$) is always 50.9%, and hence the height variation in the side view would be larger especially in the central printed region (inner loops), compared with the proposed ASAD method. A profile example based on the linear spacing with constant w_x in the side view is shown in Figure 70.

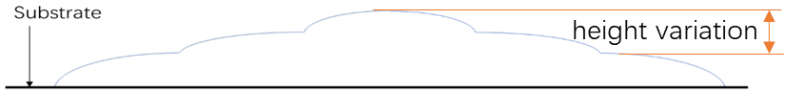

(a)

(b)

Figure 70. (a) Illustration (b) profile example based on the linear spacing with constant w_x in the side view.

In Figure 71, it can be seen that the filled rate could be close to 100 percent for a large radius of the printed pattern. Therefore, the feasibility of the proposed

strategy was verified at different printing ratios (the printed circle radius to the deposition radius $\frac{R}{w_0}$).

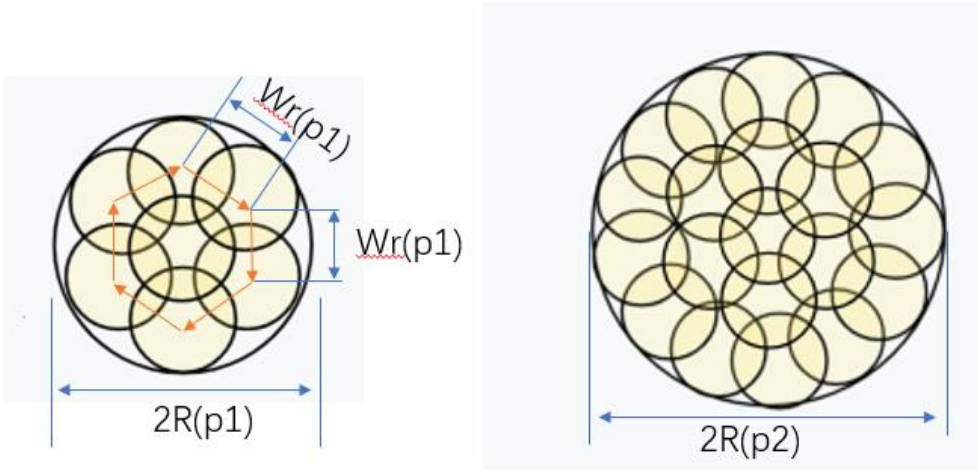

Figure 71. Deposition points based on the proposed ASAD method, for different printed radii.

As shown in Figure 72, as the printing ratio $\frac{R}{w_0}$ becomes larger, the angular displacement becomes smaller and the filled rate increases based on the ASAD method.

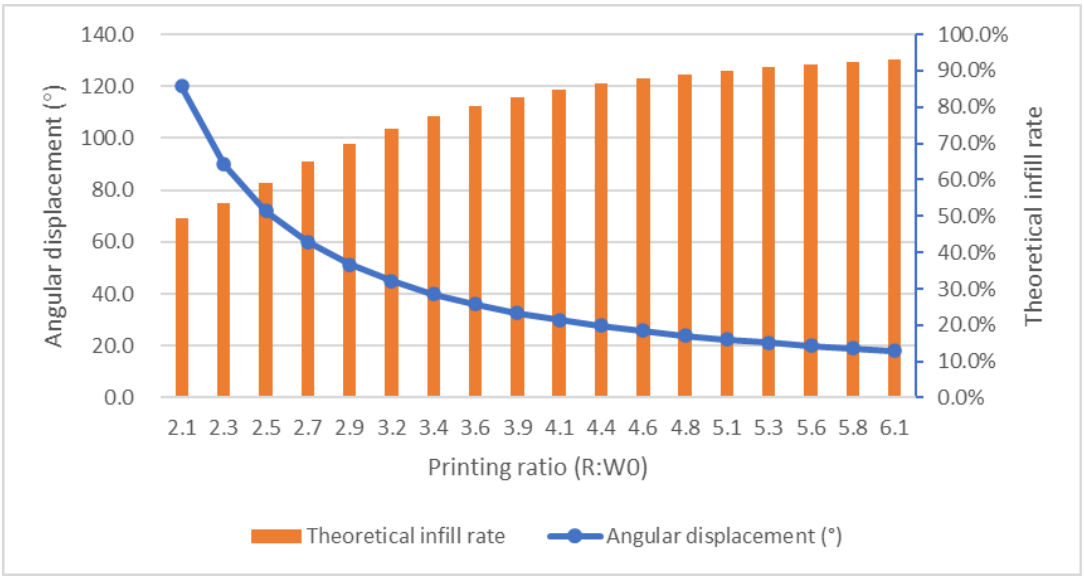

Figure 72. Relationships among the filled rate, the angular displacement and the printing ratio.

As shown in Figure 73 (a), the results based on the deposition points in Figure 73 (b) were analyzed by ImageJ software. According to the ASAD method, $w_r(p1)$ is 1.71 mm, using Figure 46 as a reference.

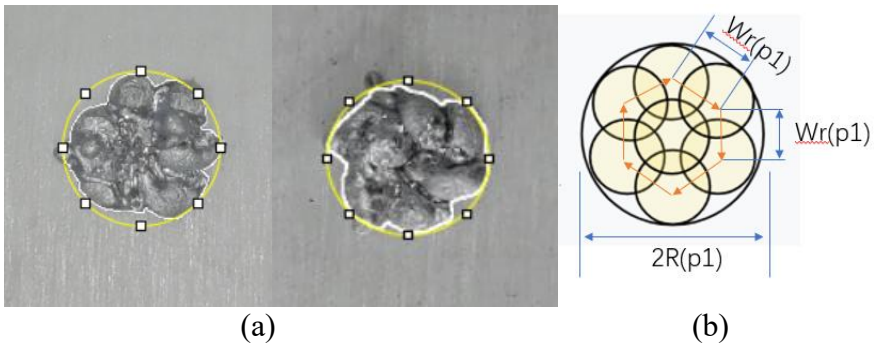

Figure 73. (a) Results, (b) deposition points in circular pattern with printing ratio of 2.7 based on ASAD.

As droplets at 900 degrees were deposited onto the substrate at 400 degrees, the droplets were fluid at the moment of deposition, and the overlapping part flowed around. As a result, the average filled rate 75.1% is relatively larger than the theoretical value. For printing curved patterns with small radii, small deflections would have a great impact on printing quality.

Based on the proposed ASAD method, the deposition points at the printing ratio of 4.6 are displayed in Figure 74 (a). On the optimized trajectory, w_{r1} was less than w_{r2} for a smoother surface in the profile. According to the adaptive spacings for the corresponding arcs in the ASAD method, w_{r1} is 1.60 mm and w_{r2} is 1.71 mm, using Figure 46 as a reference.

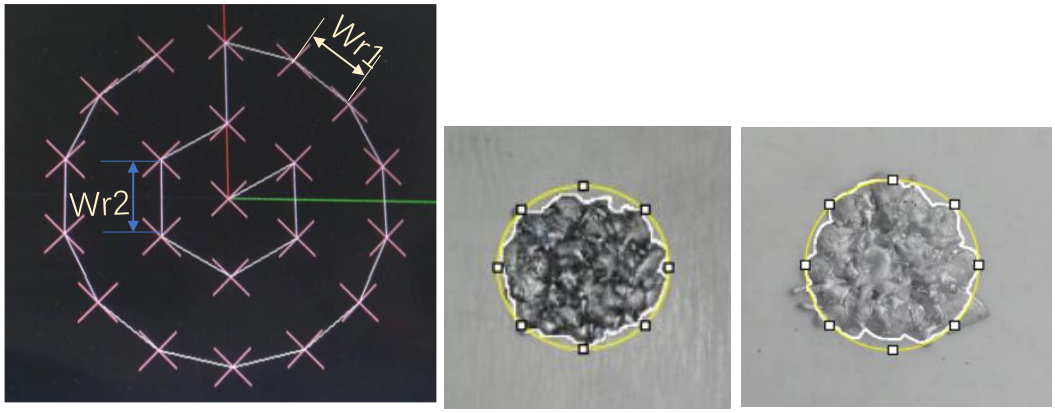

(a) (b)

Figure 74. (a) Deposition points, (b) results in circular pattern with printing ratio of 4.6 based on ASAD.

The results at the printing ratio of 4.6 in Figure 74 (b) show that the average filled rate is 88.2%, which agrees with the theoretical filled rate. The heights in profile based on the different filling strategies are shown in Figure 75, and the height variations for the zigzag, contour and ASAD methods are 0.25, 0.24 and 0.15 mm respectively. The result shows that the ASAD method, with a high accuracy of approximating curved contours, improves the surface flatness by 37.5% and 40.0% compared to the contour and zigzag paths respectively.

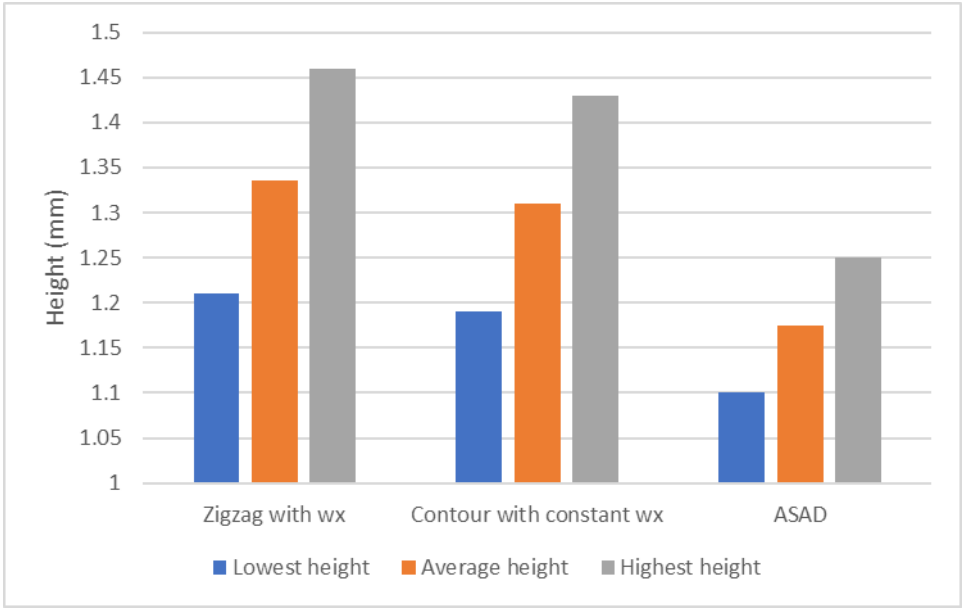

Figure 75. Heights in profile using the different filling strategies.

Without the optimized angular displacement for each loop, there may be a remaining angle insufficient for a droplet to be deposited in the contour path with the constant droplet spacing w_x, as shown in Figure 76 (a). For the contour closure, the number of deposited droplets for the loop was changed in Figure 76 (b), resulting in a greater height variation in the profile.

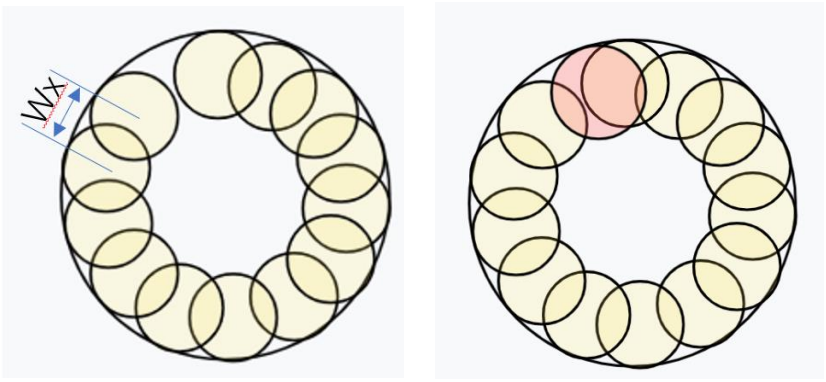

(a) (b)

Figure 76. (a) Remaining angle in contour path with constant w_x, (b) deposited droplets for contour closure.

In addition, the overlap rate was high in the contour path with the constant droplet spacing w_x, excessive droplets were deposited in the loops when printing objects with the same cross-sectional area size, as shown in Figure 77. Therefore, the increase in the profile height was significant when printing in the inner loops, compared with the deposition points in Figure 73 (b). Uneven surfaces were not conducive to the deposition of upper layers, and hence the printed structures based on the conventional contour path were unstable, causing tilting or collapsing.

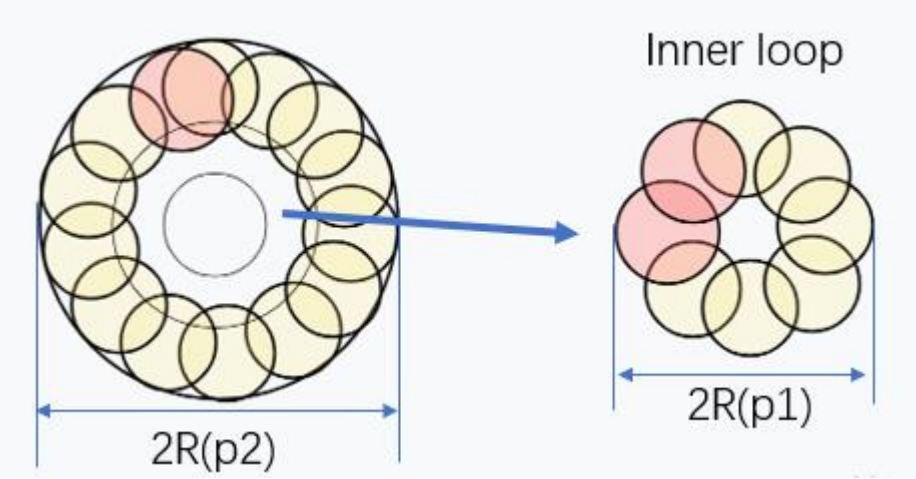

Figure 77. Deposition points in the inner loop with the constant droplet spacing w_x.

Based on the ASAD method, cylinders were printed for testing. The side view of a printed cylinder is shown in Figure 78, and the deflection in the vertical direction was similar to the column cases in Figure 18. Since the upper layers were situated away from the substrate, most of the droplets in the upper layers belong to mechanical connections.

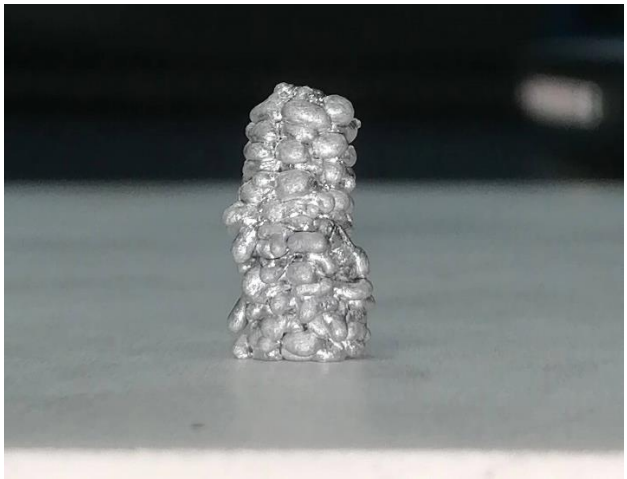

Figure 78. Side view of a printed cylinder.

The average height of the printed cylinders is within the range of 14.7 to 15.1 mm, which has a small variation in height at the top surface. For the strength analysis, the compression test was performed on the printed cylinders by the

Universal Testing Machine with the compression velocity of 3 mm/min. As shown in Figure 79, the compression load-strain relationship suggests elastic deformation in the range of 0 to 0.02 mm. According to 0.2% offset of the gauge length, the average yield strength is 655 kPa, due to the mechanical connections in the upper layers.

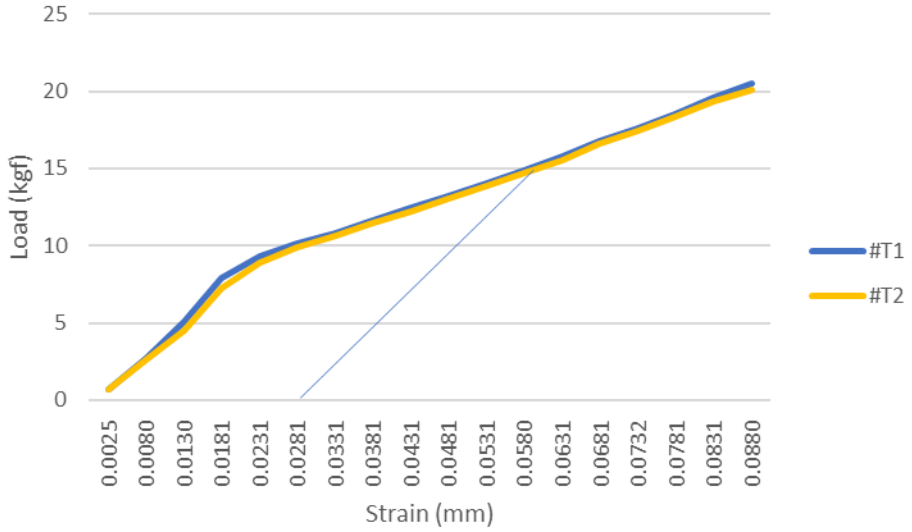

Figure 79. Compression load-strain relationship.

Heating during the printing process can improve adhesion. As a result of this, the upper layers will be in more metallurgical bonding if the substrate temperature is higher. In the project, the substrate could be heated to 400 ℃. It was difficult to increase the substrate temperature above 400 degrees, since the heating power of the substrate was basically equal to the heat dissipation over 400 degrees. If the substrate structure is redesigned for a higher temperature, better bonding of metal droplets can be achieved.

Chapter 5 Conclusion

5.1 Summary of the work

In the study, the path planning process was optimized to print the curved shapes additively. The printing system components (including the moving and deposition part, and the heating part) for high-melting-point metals were integrated, and therefore the system operation was supported in the compatible software and hardware. Based on the current experimental system and optimization strategies, the following main points were demonstrated. (a) Molten aluminum droplets can be generated and deposited on demand, and this is reproducible. (b) The two-dimensional curved shapes can be internally filled without visible voids, and the surface quality can be superior compared to the other methods. (c) Three-dimensional parts can be fabricated with a height more than 10 mm.

The developed approach is feasible for the droplet landing, and therefore, this will be of great significance for the study of different droplets in the printing of 2D or 3D curved shapes. In the present work, depending on the contour closure, the corresponding angles between neighboring droplets are compensated to achieve the equal angular displacement. In addition, the droplet spacing is adaptive for various curvatures and loops with the internal filling, and the reasonable number of droplets for each loop can be determined. Therefore, in the project, the spacings such as 1.60 mm and 1.71 mm were calculated for the corresponding loops with various curvatures. The surface flatness of printed objects was improved by 37.5% to 40.0% based on the proposed strategy compared to the commonly used path patterns, and the accuracy of approximating curved contours was relatively high, close to 90%. Comparison with the conventional paths proves its advantages in fabrication, and the feasibility was verified. The optimized printing parameters have a positive effect on the surface flatness, which is conducive to the upper layer deposition in 3D printing. For the internal filling of 3D objects with curved contours, good surface quality can be achieved with the void size reduction, in the balancing of improving dimensional accuracy and reducing material consumption. In the

software processing of the deposition paths, the designed program can simplify the operational steps in additive manufacturing, and the output motion commands can be applied to 3D printers or other industrial robots based on G programming language. In conclusion, the strategies proposed in this study can promote the practical application of droplet fabrication techniques to some extent.

5.2 Project outlook

In the adaptive spacing strategy proposed in this study, the aluminum droplets themselves are sized between the micron and millimetre scale, and the small size variations in the combination of neighbouring droplets are simplified to the ideal fusion of the droplets. The energy conversion of the droplet combination may lead to inhomogeneous expansion and contraction at the bonding interface, causing the bonding shape of the droplet to be non-ideal, and potentially creating protrusions or dimples at the bonding interface [85]. This may influence the spreading of the neighbouring droplets, affecting the combination in the printing. The substrate temperature or the heated droplet temperature can be adjusted to reduce possible fusion defects [86]. Additionally, the surface of the droplets was in contact with the outside environment, associated with the oxidation [87]. The formation of the oxide layer may also affect the combination of neighbouring droplets to a certain extent. Therefore, it is recommended that the printing system is placed in a protective gas environment that is close to oxygen-free.

In the future research, the stability of creating smaller sized droplets will be tested, and the deposition deflection is required to be minimized. Depending on the different areas to be printed, droplets of various sizes can be deposited, and therefore, path strategies can be further optimized. More experiments of other high melting point metals can be conducted for manufacturing composite materials, superior to original components. Better structural strength and dimensional accuracy can be obtained by selecting the optimal combination of layer thicknesses and the pause time between the depositions of two successive droplets.

For more accurate motion position compensation, cameras or sensors can be mounted at the corners or above the 3D stage to detect positional feedback. The error in the motion platform can be compensated by hardware or software [88]. When the 3D stage is repositioned, the position arrival signal can be transmitted to the controller and the droplets can be generated. The closed-loop control allows the droplets to deposit on the substrate at the same position as set by the software, improving the expected printing accuracy. In addition, available degrees of freedom in the motion stage can be increased, and hence the substrate can be tilted. As a result, molten metal droplets can be deposited to form objects with different tilted shapes. In the future, all operating commands can be transmitted remotely and wirelessly via cloud services. Based on the automated printing and remote control of additive manufacturing, manufacturing safety can be further improved.

References

[1] S. H. Huang, P. Liu, A. Mokasdar, and L. Hou, "Additive manufacturing and its societal impact: a literature review," *The International Journal of Advanced Manufacturing Technology*, vol. 67, no. 5-8, pp. 1191-1203, 2012, doi: 10.1007/s00170-012-4558-5.

[2] M. Mehrpouya, A. Dehghanghadikolaei, B. Fotovvati, A. Vosooghnia, S. S. Emamian, and A. Gisario, "The Potential of Additive Manufacturing in the Smart Factory Industrial 4.0: A Review," *Applied Sciences*, vol. 9, no. 18, 2019, doi: 10.3390/app9183865.

[3] G. Prashar, H. Vasudev, and D. Bhuddhi, "Additive manufacturing: expanding 3D printing horizon in industry 4.0," *International Journal on Interactive Design and Manufacturing (IJIDeM)*, 2022, doi: 10.1007/s12008-022-00956-4.

[4] N. Singh *et al.*, "Recent Advancements in Additive Manufacturing (AM) Techniques: A Forward-Looking Review," *Metals and Materials International*, 2023, doi: 10.1007/s12540-022-01380-9.

[5] S. I. Yanez-Sanchez, M. D. Lennox, D. Therriault, B. D. Favis, and J. R. Tavares, "Model Approach for Binder Selection in Binder Jetting," *Industrial & Engineering Chemistry Research*, vol. 60, no. 42, pp. 15162-15173, 2021, doi: 10.1021/acs.iecr.1c02856.

[6] F. Fina *et al.*, "3D printing of drug-loaded gyroid lattices using selective laser sintering," *Int J Pharm*, vol. 547, no. 1-2, pp. 44-52, Aug 25 2018, doi: 10.1016/j.ijpharm.2018.05.044.

[7] M. Vaezi, H. Seitz, and S. Yang, "A review on 3D micro-additive manufacturing technologies," *The International Journal of Advanced Manufacturing Technology*, vol. 67, no. 5-8, pp. 1721-1754, 2012, doi: 10.1007/s00170-012-4605-2.

[8] R. B. Kristiawan, F. Imaduddin, D. Ariawan, Ubaidillah, and Z. Arifin, "A review on the fused deposition modeling (FDM) 3D printing: Filament processing, materials, and printing parameters," *Open Engineering*, vol. 11, no. 1, pp. 639-649, 2021, doi: 10.1515/eng-2021-0063.

[9] J. C. Steuben, A. P. Iliopoulos, and J. G. Michopoulos, "Implicit slicing for functionally tailored additive manufacturing," *Computer-Aided Design*, vol. 77, pp. 107-119, 2016, doi: 10.1016/j.cad.2016.04.003.

[10] F. Gao and A. A. Sonin, "Precise deposition of molten microdrops: the physics of digital microfabrication," *Proceedings of the Royal Society of London. Series A: Mathematical and Physical Sciences*, vol. 444, pp. 533 - 554, 1994.

[11] J. Luo, L. Qi, Y. Tao, Q. Ma, and C. W. Visser, "Impact-driven ejection of micro metal droplets on-demand," *International Journal of Machine Tools and Manufacture,* vol. 106, pp. 67-74, 2016/07/01/ 2016, doi: https://doi.org/10.1016/j.ijmachtools.2016.04.002.

[12] Y. Dou, J. Luo, L. Qi, H. Lian, and J. Huang, "Drop-on-demand printing of recyclable circuits by partially embedding molten metal droplets in plastic substrates," *Journal of Materials Processing Technology,* vol. 297, p. 117268, 2021/11/01/ 2021, doi: https://doi.org/10.1016/j.jmatprotec.2021.117268.

[13] M. Simonelli *et al.*, "Towards digital metal additive manufacturing via high-temperature drop-on-demand jetting," *Additive Manufacturing,* vol. 30, p. 100930, 2019/12/01/ 2019, doi: https://doi.org/10.1016/j.addma.2019.100930.

[14] M. Meda, P. Mehta, C. Mahajan, B. Kahn, and D. Cormier, "Magnetohydrodynamic liquid metal droplet jetting of highly conductive electronic traces," *Flexible and printed electronics,* vol. 6, no. 3, 2021, doi: 10.1088/2058-8585/ac0fee.

[15] P. M. Pandey, N. V. Reddy, and S. G. Dhande, "Slicing procedures in layered manufacturing: a review," *Rapid Prototyping Journal,* vol. 9, pp. 274-288, 2003.

[16] Z. Zhao and Z. Luc, "Adaptive direct slicing of the solid model for rapid prototyping," *International Journal of Production Research,* vol. 38, no. 1, pp. 69-83, 2000/01/01 2000, doi: 10.1080/002075400189581.

[17] R. M. M. H. Gregori, N. Volpato, R. Minetto, and M. V. G. D. Silva, "Slicing Triangle Meshes: An Asymptotically Optimal Algorithm," in *2014 14th International Conference on Computational Science and Its Applications*, 30 June-3 July 2014 2014, pp. 252-255, doi: 10.1109/ICCSA.2014.58.

[18] M. Šljivić, A. Pavlović, M. Kraišnik, and J. Ilić, "Comparing the accuracy of 3D slicer software in printed enduse parts," *IOP Conference Series: Materials Science and Engineering,* vol. 659, 2019.

[19] P. Nayyeri, K. Zareinia, and H. Bougherara, "Planar and nonplanar slicing algorithms for fused deposition modeling technology: a critical review," *The International Journal of Advanced Manufacturing Technology,* vol. 119, no. 5, pp. 2785-2810, 2022/03/01 2022, doi: 10.1007/s00170-021-08347-x.

[20] J. Liu, Y. Fan, Q. Lu, and Y. Yang, "Design of extendable Tool Path Generation software for 3D printing," in *2014 International Conference on Manipulation, Manufacturing and Measurement on the Nanoscale (3M-NANO)*, 27-31 Oct. 2014 2014, pp. 130-133, doi: 10.1109/3M-NANO.2014.7057354.

[21] J. Werner, M. Aburaia, A. Raschendorfer, and M. Lackner, "MeshSlicer: A 3D-Printing software for printing 3D-models with a 6-axis industrial robot," *Procedia CIRP*, vol. 99, pp. 110-115, 2021/01/01/ 2021, doi: https://doi.org/10.1016/j.procir.2021.03.018.

[22] Y. Li, K. Xu, X. Liu, M. Yang, J. Gao, and P. Maropoulos, "Stress-oriented 3D printing path optimization based on image processing algorithms for reinforced load-bearing parts," *CIRP Annals*, vol. 70, no. 1, pp. 195-198, 2021/01/01/ 2021, doi: https://doi.org/10.1016/j.cirp.2021.04.037.

[23] L. J. Nowak and E. Pawlowska, "Technical Note: an algorithm and software for conversion of radiotherapy contour-sequence data to ready-to-print 3D structures," *Medical Physics*, vol. 46, no. 4, pp. 1829-1832, 2019/04/01 2019, doi: https://doi.org/10.1002/mp.13452.

[24] C. R. Garcia, R. C. Rumpf, H. H. Tsang, and J. H. Barton, "Effects of extreme surface roughness on 3D printed horn antenna," *Electronics letters*, vol. 49, no. 12, pp. 734-736, 2013, doi: 10.1049/el.2013.1528.

[25] H.-s. Zuo, H.-j. Li, L.-h. Qi, J. Luo, S.-y. Zhong, and H.-p. Li, "Effect of wetting behavior on generation of uniform aluminum droplets obtained by pneumatic drop-on-demand technique," *Journal of Materials Processing Technology*, vol. 214, no. 11, pp. 2566-2575, 2014/11/01/ 2014, doi: https://doi.org/10.1016/j.jmatprotec.2014.05.017.

[26] H. Yi, L. Qi, J. Luo, D. Zhang, and N. Li, "Direct fabrication of metal tubes with high-quality inner surfaces via droplet deposition over soluble cores," *Journal of Materials Processing Technology*, vol. 264, pp. 145-154, 2019/02/01/ 2019, doi: https://doi.org/10.1016/j.jmatprotec.2018.09.004.

[27] Y.-a. Jin, Y. He, G.-h. Xue, and J.-z. Fu, "A parallel-based path generation method for fused deposition modeling," *The International Journal of Advanced Manufacturing Technology*, vol. 77, no. 5, pp. 927-937, 2015/03/01 2015, doi: 10.1007/s00170-014-6530-z.

[28] S. C. Park and B. K. Choi, "Tool-path planning for direction-parallel area milling," *Computer-Aided Design*, vol. 32, no. 1, pp. 17-25, 2000/01/01/ 2000, doi: https://doi.org/10.1016/S0010-4485(99)00080-9.

[29] Y. Jin, Y. He, G. Fu, A. Zhang, and J. Du, "A non-retraction path planning approach for extrusion-based additive manufacturing," *Robotics and Computer-Integrated Manufacturing*, vol. 48, pp. 132-144, 2017/12/01/ 2017, doi: https://doi.org/10.1016/j.rcim.2017.03.008.

[30] H. Wei, K. Deng, Y. Tan, and W. Liu, "A Motion State-based Printing Time Modeling and Printing Cost Analysis for Laser Direct Deposition Process," *The International Journal of Advanced Manufacturing Technology*, vol. 114, no. 9, pp. 3109-3121, 2021/06/01 2021, doi: 10.1007/s00170-021-07064-9.

[31] F. Michel, H. Lockett, J. Ding, F. Martina, G. Marinelli, and S. Williams, "A modular path planning solution for Wire + Arc Additive Manufacturing," *Robotics and Computer-Integrated Manufacturing*, vol. 60, pp. 1-11, 2019/12/01/ 2019, doi: https://doi.org/10.1016/j.rcim.2019.05.009.

[32] Y. Jin, J. Du, Z. Ma, A. Liu, and Y. He, "An optimization approach for path planning of high-quality and uniform additive manufacturing," *The International Journal of Advanced Manufacturing Technology*, vol. 92, no. 1, pp. 651-662, 2017/09/01 2017, doi: 10.1007/s00170-017-0207-3.

[33] N. Dai, G. L. Dong, W. H. Liao, and Y. C. Sun, "Dental restoration contour-parallel offset tool path links based on graph model," *The International Journal of Advanced Manufacturing Technology*, vol. 66, no. 1, pp. 555-563, 2013/04/01 2013, doi: 10.1007/s00170-012-4349-z.

[34] Y. Yang, H. T. Loh, J. Y. H. Fuh, and Y. G. Wang, "Equidistant path generation for improving scanning efficiency in layered manufacturing," *Rapid prototyping journal*, vol. 8, no. 1, pp. 30-37, 2002, doi: 10.1108/13552540210413284.

[35] L. Ren, T. Sparks, J. Ruan, and F. Liou, "Process planning strategies for solid freeform fabrication of metal parts," *Journal of Manufacturing Systems*, vol. 27, no. 4, pp. 158-165, 2008/10/01/ 2008, doi: https://doi.org/10.1016/j.jmsy.2009.02.002.

[36] M. Biegler, J. Wang, L. Kaiser, and M. Rethmeier, "Automated Tool-Path Generation for Rapid Manufacturing of Additive Manufacturing Directed Energy Deposition Geometries," *steel research international*, vol. 91, no. 11, p. 2000017, 2020/11/01 2020, doi: https://doi.org/10.1002/srin.202000017.

[37] D. Ding, Z. Pan, D. Cuiuri, H. Li, and N. Larkin, "Adaptive path planning for wire-feed additive manufacturing using medial axis transformation," *Journal of Cleaner Production*, vol. 133, pp. 942-952, 2016/10/01/ 2016, doi: https://doi.org/10.1016/j.jclepro.2016.06.036.

[38] J. C. G. Alba, D. A. Nunez, M. Mauledoux, and O. F. Aviles, "Deposition Toolpath Pattern Comparison: Contour-Parallel and Hilbert Curve Application," *International Journal of Mechanical Engineering and Robotics Research*, pp. 542-548, 2022, doi: 10.18178/ijmerr.11.7.542-548.

[39] F. Ren, Y. Sun, and D. Guo, "Combined reparameterization-based spiral toolpath generation for five-axis sculptured surface machining," *The International Journal of Advanced Manufacturing Technology*, vol. 40, no. 7, pp. 760-768, 2009/02/01 2009, doi: 10.1007/s00170-008-1385-9.

[40] Y.-a. Jin, Y. He, G.-h. Xue, and J.-z. Fu, "A parallel-based path generation method for fused deposition modeling," *International journal of advanced manufacturing technology*, vol. 77, no. 5-8, pp. 927-937, 2015, doi: 10.1007/s00170-014-6530-z.

[41] Y.-a. Jin, Y. He, J.-z. Fu, W.-f. Gan, and Z.-w. Lin, "Optimization of tool-path generation for material extrusion-based additive manufacturing technology," *Additive manufacturing*, vol. 1-4, pp. 32-47, 2014, doi: 10.1016/j.addma.2014.08.004.

[42] Y. Zhou, K. Zhang, Y. Liang, J. Cheng, and Y. Dai, "Selective Laser Melted Magnesium Alloys: Fabrication, Microstructure and Property," *Materials*, vol. 15, no. 20, p. 7049, 2022, doi: 10.3390/ma15207049.

[43] L. E. Murr *et al.*, "Metal Fabrication by Additive Manufacturing Using Laser and Electron Beam Melting Technologies," *Journal of materials science & technology*, vol. 28, no. 1, pp. 1-14, 2012, doi: 10.1016/S1005-0302(12)60016-4.

[44] S. X. Cheng, T. Li, and S. Chandra, "Producing molten metal droplets with a pneumatic droplet-on-demand generator," *Journal of Materials Processing Technology*, vol. 159, no. 3, pp. 295-302, 2005/02/10/ 2005, doi: https://doi.org/10.1016/j.jmatprotec.2004.05.016.

[45] M. Fang, S. Chandra, and C. B. Park, "Building three-dimensional objects by deposition of molten metal droplets," *Rapid Prototyping Journal*, vol. 14, no. 1, pp. 44-52, 2008, doi: 10.1108/13552540810841553.

[46] K. Yamaguchi, K. Sakai, T. Yamanaka, and T. Hirayama, "Generation of three-dimensional micro structure using metal jet," *Precision Engineering*, vol. 24, no. 1, pp. 2-8, 2000/01/01/ 2000, doi: https://doi.org/10.1016/S0141-6359(99)00015-X.

[47] W. Cao and Y. Miyamoto, "Freeform fabrication of aluminum parts by direct deposition of molten aluminum," *Journal of Materials Processing Technology*, vol. 173, no. 2, pp. 209-212, 2006/04/10/ 2006, doi: https://doi.org/10.1016/j.jmatprotec.2005.11.028.

[48] R. Li, N. Ashgriz, S. Chandra, J. R. Andrews, and J. Williams, "Drawback During Deposition of Overlapping Molten Wax Droplets," *Journal of Manufacturing Science and Engineering*, vol. 130, no. 4, 2008, doi: 10.1115/1.2952821.

[49] D. Zhang, L. Qi, J. Luo, H. Yi, W. Xiong, and Y. Mo, "Parametric mapping of linear deposition morphology in uniform metal droplet deposition technique," *Journal of materials processing technology*, vol. 264, pp. 234-239, 2019, doi: 10.1016/j.jmatprotec.2018.08.048.

[50] R. Li, N. Ashgriz, S. Chandra, J. R. Andrews, and S. Drappel, "Coalescence of two droplets impacting a solid surface," *Experiments in Fluids*, vol. 48, no. 6, pp. 1025-1035, 2010/06/01 2010, doi: 10.1007/s00348-009-0789-0.

[51] A. Dalili, S. Chandra, J. Mostaghimi, H. T. Charles Fan, and J. C. Simmer, "Formation of liquid sheets by deposition of droplets on a surface," *Journal of Colloid and Interface Science*, vol. 418, pp. 292-299, 2014/03/15/ 2014, doi: https://doi.org/10.1016/j.jcis.2013.12.033.

[52] L.-h. Qi, Y.-p. Chao, J. Luo, J.-m. Zhou, X.-h. Hou, and H.-j. Li, "A novel selection method of scanning step for fabricating metal components based on micro-droplet deposition manufacture," *International Journal of Machine Tools and Manufacture*, vol. 56, pp. 50-58, 2012/05/01/ 2012, doi: https://doi.org/10.1016/j.ijmachtools.2011.12.002.

[53] V. Korkut and H. Yavuz, "In-Space Additive Manufacturing Based on Metal Droplet Generation Using Drop-on-Demand Technique," *Journal of Materials Engineering and Performance*, vol. 31, no. 8, pp. 6101-6111, 2022/08/01 2022, doi: 10.1007/s11665-022-06865-7.

[54] Y. Dou, J. Luo, L. Qi, H. Lian, and X. Hou, "Generation mechanism and suppression method of landing error of two successively deposited metal droplets caused by coalescence and solidification," *International Journal of Heat and Mass Transfer*, vol. 172, p. 121100, 2021/06/01/ 2021, doi: https://doi.org/10.1016/j.ijheatmasstransfer.2021.121100.

[55] M. Fang, S. Chandra, and C. B. Park, "Heat Transfer During Deposition of Molten Aluminum Alloy Droplets to Build Vertical Columns," *Journal of Heat Transfer*, vol. 131, no. 11, 2009, doi: 10.1115/1.3156782.

[56] C.-H. Wang, H.-L. Tsai, Y.-C. Wu, and W.-S. Hwang, "Investigation of molten metal droplet deposition and solidification for 3D printing techniques," *Journal of Micromechanics and Microengineering*, vol. 26, no. 9, p. 095012, 2016/07/08 2016, doi: 10.1088/0960-1317/26/9/095012.

[57] T. Horii, S. Kirihara, and Y. Miyamoto, "Freeform fabrication of superalloy objects by 3D micro welding," *Materials & Design*, vol. 30, no. 4, pp. 1093-1097, 2009/04/01/ 2009, doi: https://doi.org/10.1016/j.matdes.2008.06.033.

[58] D. Zhang, L. Qi, J. Luo, H. Yi, X. Hou, and H. Li, "Geometry control of closed contour forming in uniform micro metal droplet deposition manufacturing," *Journal of Materials Processing Technology*, vol. 243, pp. 474-480, 2017/05/01/ 2017, doi: https://doi.org/10.1016/j.jmatprotec.2017.01.007.

[59] Y. Dou, J. Luo, L. Qi, and H. Lian, "A vertex-arc path planning method for metal droplet-based 3D printing of thin-walled parts with sharp corners," *Journal of Materials Processing Technology*, vol. 312, p. 117852, 2023/03/01/ 2023, doi: https://doi.org/10.1016/j.jmatprotec.2022.117852.

[60] A. Dey and N. Yodo, "A systematic survey of FDM process parameter optimization and their influence on part characteristics," *Journal of Manufacturing and Materials Processing*, vol. 3, no. 3, p. 64, 2019, doi: 10.3390/jmmp3030064.

[61] A. a. Alafaghani, A. Qattawi, B. Alrawi, and A. Guzman, "Experimental Optimization of Fused Deposition Modelling Processing Parameters: A Design-for-Manufacturing Approach," *Procedia Manufacturing*, vol. 10, pp. 791-803, 2017, doi: 10.1016/j.promfg.2017.07.079.

[62] J. Beniak, P. Križan, Ľ. Šooš, and M. Matúš, "Research on Shape and Dimensional Accuracy of FDM Produced Parts," *IOP Conference Series: Materials Science and Engineering,* vol. 501, no. 1, p. 12030, 2019, doi: 10.1088/1757-899X/501/1/012030.

[63] S. Deswal, R. Narang, and D. Chhabra, "Modeling and parametric optimization of FDM 3D printing process using hybrid techniques for enhancing dimensional preciseness," *International journal on interactive design and manufacturing,* vol. 13, no. 3, pp. 1197-1214, 2019, doi: 10.1007/s12008-019-00536-z.

[64] M. Vishwas, C. K. Basavaraj, and M. Vinyas, "Experimental Investigation using Taguchi Method to Optimize Process Parameters of Fused Deposition Modeling for ABS and Nylon Materials," *Materials Today: Proceedings,* vol. 5, no. 2, pp. 7106-7114, 2018, doi: 10.1016/j.matpr.2017.11.375.

[65] T. Ermergen and F. Taylan, "Review on Surface Quality Improvement of Additively Manufactured Metals by Laser Polishing," *Arabian journal for science and engineering (2011),* vol. 46, no. 8, pp. 7125-7141, 2021, doi: 10.1007/s13369-021-05658-9.

[66] M. S. Alsoufi and A. E. Elsayed, "Surface Roughness Quality and Dimensional Accuracy—A Comprehensive Analysis of 100% Infill Printed Parts Fabricated by a Personal/Desktop Cost-Effective FDM 3D Printer," *Materials Sciences and Applications,* vol. 09, pp. 11-40, 2018.

[67] D. Ahn, H. Kim, and S. Lee, "Fabrication direction optimization to minimize post-machining in layered manufacturing," *International journal of machine tools & manufacture*, vol. 47, no. 3, pp. 593-606, 2007, doi: 10.1016/j.ijmachtools.2006.05.004.

[68] M. Fahad, M. Khalid, M. Nauman, and M. A. Khan, "Effect of deposition speed on the flatness and cylindricity of parts produced by three dimensional printing process," *Journal of physics. Conference series*, vol. 885, no. 1, 2017, doi: 10.1088/1742-6596/885/1/012012.

[69] N. S. A. Bakar, M. R. Alkahari, and H. Boejang, "Analysis on fused deposition modelling performance," *Journal of Zhejiang University-SCIENCE A,* vol. 11, no. 12, pp. 972-977, 2010/12/01 2010, doi: 10.1631/jzus.A1001365.

[70] P. Mishra, S. Sood, V. Bharadwaj, A. Aggarwal, and P. Khanna, "Parametric Modeling and Optimization of Dimensional Error and Surface Roughness of Fused Deposition Modeling Printed Polyethylene Terephthalate Glycol Parts," *Polymers,* vol. 15, no. 3, p. 546, 2023, doi: 10.3390/polym15030546.

[71] A. Elkaseer, S. Schneider, Y. Deng, and S. G. Scholz, "Effect of Process Parameters on the Performance of Drop-On-Demand 3D Inkjet Printing: Geometrical-Based Modeling and Experimental Validation," *Polymers,* vol. 14, no. 13, p. 2557, 2022, doi: 10.3390/polym14132557.

[72] S.-Y. Zhong, L.-H. Qi, W. Xiong, J. Luo, and Q.-X. Xu, "Research on mechanism of generating aluminum droplets smaller than the nozzle diameter by pneumatic drop-on-demand technology," *International journal of advanced manufacturing technology*, vol. 93, no. 5-8, pp. 1771-1780, 2017, doi: 10.1007/s00170-017-0484-x.

[73] S. Gong and B. He, "LabVIEW-base automatic rising and falling speed control of stepper motor," in *2009 International Conference on Electrical Machines and Systems*, 15-18 Nov. 2009 2009, pp. 1-4, doi: 10.1109/ICEMS.2009.5382704.

[74] K. Assael, Banish, R. M., Brillo, J., Egry, I., Brooks, R., Quested, P. N., Mills, K. C., Nagashima, A., Sato, Y., & Wakeham, W. A., "Reference Data for the Density and Viscosity of Liquid Aluminum and Liquid Iron," *Journal of Physical and Chemical Reference Data,* vol. 35, no. 1, pp. 285–300, 2006, doi: 10.1063/1.2149380.

[75] I. Polmear, D. StJohn, J.-F. Nie, and M. Qian, *Light Alloys : Metallurgy of the Light Metals*. Oxford, UNITED KINGDOM: Elsevier Science & Technology, 2017.

[76] F. M. a. J. C. R. V. Sarou-Kanian, "Surface Tension and Density of Oxygen-Free Liquid Aluminum at High Temperature," *International Journal of Thermophysics,* vol. 24, no. 1, pp. 277-286, 2003.

[77] H. Seli, M. Awang, A. Ismail, E. Rachman, and Z. Ahmad, "Evaluation of Properties and FEM Model of the Friction Welded Mild Steel-Al6061-Alumina," *Materials Research,* vol. 16, pp. 453-467, 04/01 2013, doi: 10.1590/S1516-14392012005000178.

[78] C. P. Kothandaraman, *Fundamentals of heat and mass transfer [electronic resource] / C.P. Kothandaraman,* Rev. 3rd ed. ed. New Delhi: New Delhi : New Age International P Ltd., Publishers, pp. 357-358, 2006.

[79] S. Chandra and C. T. Avedisian, "On the collision of a droplet with a solid surface," *Proceedings of the Royal Society of London. Series A: Mathematical and Physical Sciences,* vol. 432, no. 1884, pp. 13-41, 1997/01/01 1997, doi: 10.1098/rspa.1991.0002.

[80] M. Pasandideh-Fard, Y. M. Qiao, S. Chandra, and J. Mostaghimi, "Capillary effects during droplet impact on a solid surface," *Physics of Fluids,* vol. 8, no. 3, pp. 650-659, 1996, doi: 10.1063/1.868850.

[81] S. Schiaffino and A. A. Sonin, "Molten droplet deposition and solidification at low Weber numbers," *Physics of Fluids,* vol. 9, no. 11, pp. 3172-3187, 1997, doi: 10.1063/1.869434.

[82] Y. Liu, P. Tan, and L. Xu, "Kelvin Helmholtz instability in an ultrathin air film causes drop splashing on smooth surfaces," 2015, doi: 10.1073/pnas.1417718112.

[83] H. Yi, L.-h. Qi, J. Luo, Y. Jiang, and W. Deng, "Pinhole formation from liquid metal microdroplets impact on solid surfaces," *Applied Physics Letters*, vol. 108, no. 4, p. 041601, 2016, doi: 10.1063/1.4940404.

[84] H. Li, P. Wang, L. Qi, H. Zuo, S. Zhong, and X. Hou, "3D numerical simulation of successive deposition of uniform molten Al droplets on a moving substrate and experimental validation," *Computational Materials Science*, vol. 65, pp. 291-301, 2012/12/01/ 2012, doi: https://doi.org/10.1016/j.commatsci.2012.07.034.

[85] H. Yi, L. Qi, J. Luo, D. Zhang, H. Li, and X. Hou, "Effect of the surface morphology of solidified droplet on remelting between neighboring aluminum droplets," *International Journal of Machine Tools and Manufacture*, vol. 130-131, pp. 1-11, 2018/08/01/ 2018, doi: https://doi.org/10.1016/j.ijmachtools.2018.03.006.

[86] S. Li, Z. Wei, J. Du, P. Wei, Z. Hou, and B. Lu, "The fusion process of successive droplets impinging onto a substrate surface," *Applied Physics A*, vol. 120, no. 1, pp. 35-42, 2015/07/01 2015, doi: 10.1007/s00339-015-9146-8.

[87] D. Rumschoettel, B. Griebel, F. Irlinger, and T. C. Lueth, "A fast pneumatic droplet generator for the ejection of molten aluminum," 2017: SMTA, pp. 1-8.

[88] Z. Ge, H. Chen, and X. Han, "Accuracy analysis and errors compensation of 4-DOF reconfigurable punching robot," *IOP Conference Series: Materials Science and Engineering*, vol. 892, p. 012081, 08/04 2020, doi: 10.1088/1757-899X/892/1/012081.